Remote Sensing of Environment 231 (2019) 111238

Contents lists available at ScienceDirect

Remote Sensing of Environment

journal homepage: www.elsevier.com/locate/rse

Integrating multi-sensor remote sensing and species distribution modeling to map the spread of emerging forest disease and tree mortality

Yinan He[a], Gang Chen[a,*], Christopher Potter[b], Ross K. Meentemeyer[c,d]

[a] Laboratory for Remote Sensing and Environmental Change (LRSEC), Department of Geography and Earth Sciences, University of North Carolina at Charlotte, 9201 University City Blvd, Charlotte, NC 28223, USA
[b] NASA Ames Research Center, Moffett Field, CA 94035, USA
[c] Center for Geospatial Analytics, North Carolina State University, 3120 Jordan Hall, Raleigh, NC 27695, USA
[d] Department of Forestry and Environmental Resources, North Carolina State University, 3120 Jordan Hall, Raleigh, NC 27695, USA

ARTICLE INFO

Edited by Jing M. Chen

Keywords:
Multi-sensor remote sensing
Species distribution model
Emerging infectious disease (EID)
Spectral unmixing
Landscape epidemiology
Object-based image analysis
Sudden oak death

ABSTRACT

Forest ecosystems have been increasingly affected by a variety of disturbances, including emerging infectious diseases (EIDs), causing extensive tree mortality in the Western United States. Especially over the past decade, EID outbreaks occurred more frequently and severely in forest landscapes, which have killed large numbers of trees. While tree mortality is observable from remote sensing, its symptom may be associated with both disease and non-disease disturbances (e.g., wildfire and drought). Species distribution modeling is widely used to understand species spatial preferences for certain habitat conditions, which may constrain uncertain remote sensing approaches due to limited spatial and spectral resolution. In this study, we integrated multi-sensor remote sensing and species distribution modeling to map disease-caused tree mortality in a forested area of 80,000 ha from 2005 to 2016. We selected sudden oak death (caused by pathogen *P. ramorum*) as a case study of a rapidly spreading emerging infectious disease, which has killed millions of oak (*Quercus* spp.) and tanoak (*Lithocarpus densiflorus*) in California over the past decades. To balance the needs for fine-scale monitoring of disease distribution patterns and satisfactory coverage at broad scales, our method applied spectral unmixing to extract sub-pixel disease presence using yearly Landsat time series. The results were improved by employing the probability of disease infection generated from a species distribution model. We calibrated and validated the method with image samples from high-spatial resolution NAIP (National Agriculture Imagery Program), and hyperspectral AVIRIS (Airborne Visible/Infrared Imaging Spectrometer) sensors, Google Earth® imagery, and field observations. The findings reveal an annual sudden oak death infection rate of 7% from 2005 to 2016, with overall mapping accuracies ranging from 76% to 83%. The integration of multi-sensor remote sensing and species distribution modeling considerably reduced the overestimation of disease effects as compared to the use of remote sensing alone, leading to an average of 26% decrease in detecting disease-affected trees. Such integration strategy proved the effectiveness of mapping long-term, disease-caused tree mortality in forest landscapes that have experienced multiple disturbances.

1. Introduction

Forests play a pivotal role in regulating the energy and mass exchange between terrestrial ecosystems and the atmosphere (Likens et al., 1981). However, environmental disturbances, including those caused by emerging infectious diseases (EIDs) of plants, are beginning to impact the biodiversity, structure, and functioning of forest ecosystems in new ways (Anderegg et al., 2013). Especially over the past decade, EID outbreaks occurred more frequently and severely in forest landscapes, which have contributed to unprecedented tree mortality (Asner, 2013; Boyd et al., 2013; Wingfield et al., 2015; Chen and Meentemeyer, 2016).

Remote detection of EID-caused tree mortality can be an efficient and accurate method to scale up field measurements to the landscape scale (Chen and Meentemeyer, 2016; Hultquist et al., 2014; Kelly et al., 2004; Liu et al., 2007). Mapping pathogen-related disturbances allows stakeholders to prioritize management actions at particular locations of concern, often over large areas (e.g., Meentemeyer et al., 2015). Successful detection relies on the fact that infected trees show distinct spectral, spatial and/or temporal symptoms, which may be related to

* Corresponding author.
E-mail address: gang.chen@uncc.edu (G. Chen).

https://doi.org/10.1016/j.rse.2019.111238
Received 4 December 2018; Received in revised form 27 May 2019; Accepted 1 June 2019

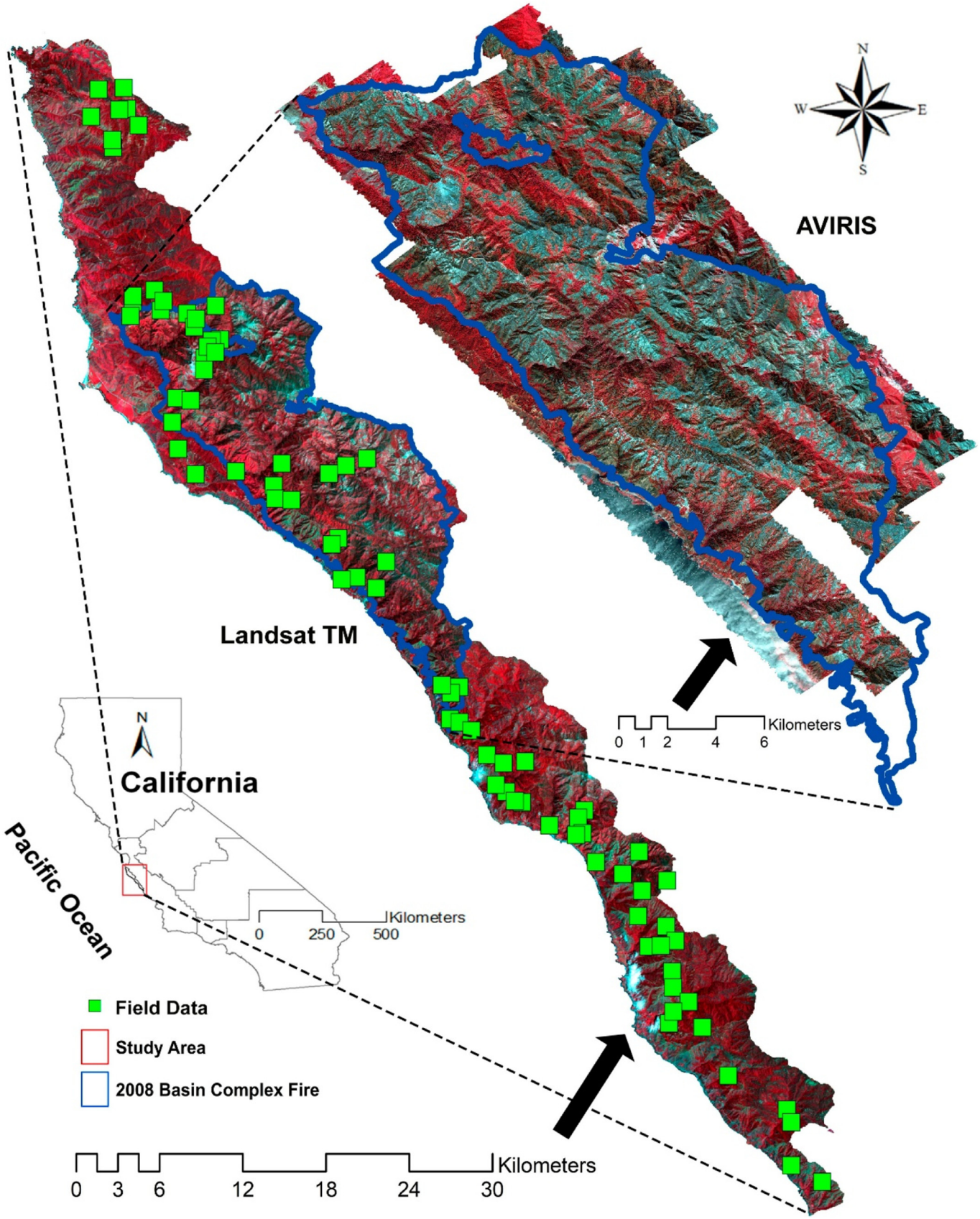

Fig. 1. Study area located in the Big Sur ecoregion on the western flank of the Santa Lucia Mountains in California. The Landsat TM (Thematic Mapper) image is from a false color composite using bands 4 (NIR), 3 (Red) and 2 (Green). The AVIRIS (Airborne Visible InfraRed Imaging Spectrometer) image is from a false color composite using bands 51 (NIR), 33 (Red), and 22 (Green). (For interpretation of the references to color in this figure legend, the reader is referred to the web version of this article.)

declines in chlorophyll/water content in foliage, leaf discoloration, defoliation, or treefall gaps [see a review by Chen and Meentemeyer, 2016]. For example, blister rust (caused by pathogen *Cronartium ribicola*) can turn the needles of eastern white pines into yellow then rusty red (Hatala et al., 2010). Oak trees appear to be 'freeze-dried' because of sudden oak death, which is caused by pathogen *Phytophthora ramorum* (Kelly and Meentemeyer, 2002). Today, sudden oak death has reached epidemic levels in many forests of the Pacific U. S. Coast, killing large numbers of oak and tanoak trees. Similar to EID-caused tree mortality mapping, there is a plethora of literature on remote detection of tree mortality, caused by environmental disturbances of drought (Brodrick and Asner, 2017; Byer and Jin, 2017; Paz-Kagan et al., 2017), outbreaks of insects (Bright et al., 2012; Fassnacht et al., 2014; Meddens et al., 2013; Pasquarella et al., 2017; Rullan-Silva et al., 2013), invasive species (Ghulam et al., 2014; Rocchini et al., 2015; Skowronek et al., 2017), and wind (McDowell et al., 2018; Negrón-Juárez et al., 2018). However, studies have rarely investigated how to identify tree mortality relevant to specific causes if multiple disturbances jointly occur in the same region. This is particularly true for areas affected by EIDs. The outbreak of EIDs is typically chronic stress spanning years to decades, which possibly overlaps with discrete events, such as severe drought and wildfire, co-occurring in the same region. Damaged trees that are caused by different disturbance types may exhibit similar (i.e., subtle discrepancies in) spectral or spatial symptoms, challenging the use of popular remotely sensed datasets, such as Landsat and MODIS data. While recent high-spatial and high-spectral resolution imagery has demonstrated the potential to uncover the subtle discrepancies to improve disease mapping (e.g., Hatala et al., 2010; Meddens et al., 2011; Vaughn et al., 2018), these data types remain costly and are scarce in spatial coverage hindering long-term monitoring of EID-caused tree mortality in any particular region of interest.

Species distribution modeling (SDM; a.k.a., environmental niche modeling) has been widely used in ecology and conservation biology to predict the statistical probability of species dispersal patterns over space and time (Elith and Leathwick, 2009). The performance of those modeling approaches depends on the abiotic conditions and the distribution of sampled observations, which are critical for effective model training and validation (Václavík and Meentemeyer, 2009). Despite its popularity, SDM may lead to high uncertainties and spurious results without reliable knowledge of the actual species (e.g., invasive pathogen) range, acquired typically through field surveys (Carneiro et al., 2016). This becomes a critical issue for estimation of EID outbreaks in forests, where the traditional inventory approaches are not logistically feasible to acquire a sufficient number of pathogen distribution samples.

To effectively map EID-caused tree mortality, bridging remote sensing and ecological SDM offers a potential solution. While such integration strategy has demonstrated to be effective in recent studies of species modeling (e.g., Saatchi et al., 2008; K.S. He et al., 2015), remote sensing is typically used to generate land cover and other ecological variables (e.g., NDVI) serving as input of SDM. For EID-caused tree mortality mapping, would it possible to apply SDM to refine remote sensing generated maps? While remote sensing approaches are likely to overestimate disease effects due to high spectral/spatial similarities across the damaged trees by EID and non-EID disturbances, SDM can provide essential knowledge informing the likelihood that certain disease disturbance may or may not occur at specific locations. This will ultimately reduce uncertainties in remote sensing-based estimation by providing an effective constraint to exclude the regions, where the studied EID has a low likelihood to occur. Integrating remote sensing and species distribution modeling particularly benefits long-term monitoring, where EIDs demonstrate a strong spatial progression pattern.

The main goal of our study was to develop a mapping method that can capture long-term, spatiotemporal patterns of EID-caused tree mortality in forest landscapes. The method integrated multi-senor remote sensing and SDM, and was developed to study sudden oak death, a rapidly spreading EID that has killed millions of trees in California and Oregon since being discovered during the mid-1990s (Rizzo et al., 2002).

2. Study area

Our study site (centered at: 36°16′ N, 121°44′ W) is located in the Big Sur, California ecoregion on the west coast of the United States. It covers an area of about 80,000 ha on the steepest coastal mountains with elevations reaching 1600 m within 4.5 km of the coast (Fig. 1). This region has a Mediterranean-type climate with moderate temperatures, mean monthly temperatures at sea level range from 10–13 °C in the winter months to 16–18 °C in the summer (Davis et al., 2010). Major forest types include mixed oak woodlands consisting of coast live oak (*Quercus agrifolia*), Shreve's oak (*Quercus parvula* var. *shrevei*), California bay laurel (*Umbellularia californica*), and Pacific madrone (*Arbutus menziesii*), as well as mixed coniferous forests, which are composed primarily of ponderosa pine (*Pinus ponderosa*), sugar pine (*Pinus lambertiana*), Jeffrey pine (*Pinus jeffreyi*), coulter pine (*Pinus coulteri*), and Santa Lucia Fir (*Abies bracteata*). They give way to riverside corridors of redwood/tanoak (*Sequoia sempervirens/Notholithocarpus densiflorus*) dominated forests at lower elevations (Davis et al., 2010). Current anthropogenic land use is still limited and consists primarily of isolated houses, roads and trails, which were used primarily for recreation within the study domain.

Sudden oak death (caused by pathogen *P. ramorum*) was first associated with mortality of tanoak (*Lithocarpus densiflorus*) and oak (*Quercus* spp.) in the San Francisco Bay region during the mid-1990s (Rizzo et al., 2002). It was quickly introduced to California and Oregon forests mainly by infested nursery stock (Davidson et al., 2005; Ivors et al., 2006; Prospero et al., 2007). Following the introduction, sudden oak death reached epidemic levels in many coastal forests and has affected large, but unknown numbers of oak and tanoak trees (Rizzo et al., 2005). Due to the aggressive transmission of the pathogen, 14 states in the U.S. imposed strict regulations for plant materials imported from the west coast, including California and Oregon (Alexander, 2012). Globally, *P. ramorum* was either listed as a regulated species or specified in national forest legislations in 68 countries (Sansford et al., 2008; Hunter et al., 2018). Although sudden oak death is the main disturbance in Big Sur, two other agents – drought and fire, have also affected the forests as major disturbances. For example, the 2012–2015 severe drought in California has led to significant water losses in forest canopies resulting in high tree mortality (Asner et al., 2016). The 2008 Basin Complex Fire, which was ignited by a dry lightning storm burned 28,383 ha within our study area (Potter, 2016).

3. Data and preprocessing

3.1. Reference data

This study has two groups of reference data: field data and remote sensing data from high-resolution Google Earth (Google, Mountain View, California) image samples and local aerial photos (NAIP, National Agriculture Imagery Program). Specifically, we have established 85 permanent field plots (50 × 50 m, 0.25 ha) since the summer of 2006 (Meentemeyer et al., 2008b). These plots were designed to follow a stratified random sampling scheme within the mixed oak woodland and redwood-tanoak (acting as the main host species of *P. ramorum*), and have been revisited yearly to monitor sudden oak death infection and its impact on forest structural change (e.g., tree density, tree height, and forest species types). A Panasonic SXBlue real-time differential GPS (Geneq, Montreal) was applied for collecting plot positions, with an average accuracy of 1.0 m or less.

To supplement the limited number of field-derived sudden oak

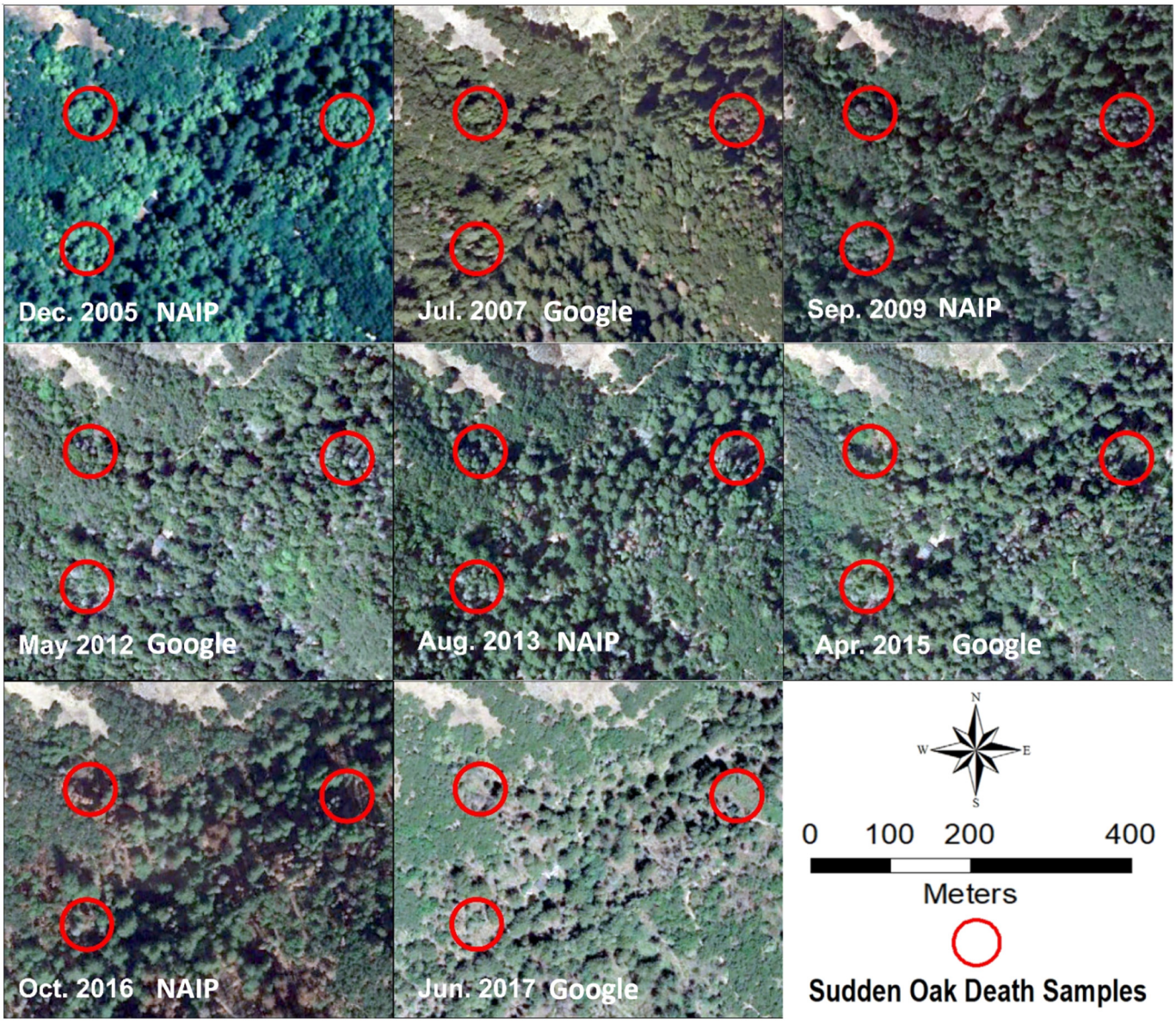

Fig. 2. Examples of isolated diseased trees being surrounded by healthy trees and symptom change over time in Google Earth and NAIP high-resolution images.

death samples, we extracted diseased and healthy tree plots from Google Earth and aerial photos (i.e., NAIP) via image interpretation. We based our interpretation on the spatial, spectral and temporal symptoms of sudden oak death-caused tree mortality in the study area that are relatively unique as compared to the drought/fire-caused tree mortality. Early in 2002, Kelly and Meentemeyer (2002) discovered the 'freeze-dried' characteristic of oak trees as a result of sudden oak death infection, and then used such spectral trait to map the spatial distribution of the disease. Fig. 2 shows examples of isolated diseased trees that are surrounded by healthy trees in multi-temporal, high-resolution true color images. Fig. 2 demonstrates the symptom changes during the three stages of sudden oak death progression (Meentemeyer et al., 2008a; Chen et al., 2015a): (i) early-stage (host trees retaining their dried foliage and fine twigs for one year or more), (ii) middle-stage (some older mortality with host trees losing fine crown fuels and surface fuels beginning to accumulate for 1–3 years), and (iii) late-stage (host trees being dead for over 4 years and causing gaps due to trees falling over). Hence, the diseased tree plots change their spatial representation over time, making it distinctive from the other disturbances in high-resolution imagery (Fig. 2).

To quantify the disease's spectral, spatial and temporal patterns as observed in Google Earth and NAIP imagery, we employed two indices. First, tree foliage dramatically changes color from healthy green to brown over one or two years following sudden oak death infection (Liu et al., 2006), and then to gray indicating foliage desiccating and pigments breakdown, leading to 'freeze-dried' appearance (Kelly and Meentemeyer, 2002). We used Red-Green Index (RGI) to capture the variation in canopy color. RGI is a simple ratio between the red and the green band. It was originally developed for detecting mountain pine beetle infestation, which causes color change in pine tree canopies (Coops et al., 2006). Using field data as reference, we calculated RGI for sunlit green, sunlit brown and sunlit gray crowns respectively. As illustrated in Fig. 3, unhealthy trees (i.e., sunlit brown and sunlit gray) are distinguishable from the healthy trees (i.e., sunlit green) with RGI locating in different value ranges.

Second, sudden oak death-caused tree mortality demonstrates isolated, patchy distribution patterns, which gradually increase the density and reduce distances to each other (Meentemeyer et al., 2008a). To analyze such patterns, we employed mean proximity index (PRO_MN) to assess the degree of isolation and fragmentation of the corresponding

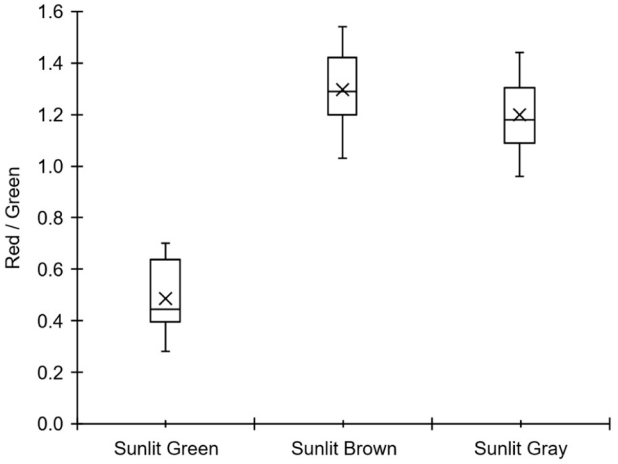

Fig. 3. Boxplots showing Red-Green Index (RGI) values (minimum, first quartile, median, mean, third quartile, and maximum) for sampled sunlit green, sunlit brown, and sunlit gray crowns.

patch type at landscape level over years (McGarigal, 2014; McGarigal and Marks, 1995). In our study, PROX_MN was used as an indicator of fragmentation for sudden oak death-caused tree mortality, with high values indicating low levels of fragmentation and low values indicating high levels of fragmentation (Turner et al., 2001).

$$\text{PROX\_MN} = \frac{\sum_{s=1}^{n} \frac{a_{ijs}}{h_{ijs}^2}}{n} \quad (1)$$

where PROX_MN represents the mean proximity index for focal patch *ij*, a_{ijs} is the area of patch *ijs* within a specified neighborhood of patch *ij*, h_{ijs} is the distance between patch *ijs* and patch *ij*, based on patch edge-to-edge distance and computed from cell center to cell center, and *n* is the total number of patches within the neighborhood. Here, PROX_MN was calculated within a neighborhood using 200 m as search radius. Our assumption is that if field data have suggested sudden oak death occurrence at that location, the neighboring trees with similar RGI values (same value range) were also affected by the disease. The neighborhood size was chosen based on our field experience in sudden oak death identification. Fig. 4 shows the trajectory of PROX_MN values over years. We did not find in the literature or in our study area that drought/fire-caused tree mortality demonstrates any specific spatial-temporal patterns over years. For example, Fig. 5 shows the trajectory of PROX_MN values for gray/brown sample areas not affected by the disease, which even indicates a decreasing trend over time.

We used 70% of the field data to estimate the range of RGI values (0.96–1.54), and the range of PROX_MN values (10.20–2509.03) and the slopes of their trend lines (63.05–196.74). The remainder of the field date was used for accuracy assessment. We have achieved an overall accuracy of 92% and a Kappa statistic of 0.84 in sudden oak death extraction from NAIP and Google Earth imagery.

Because field plots have unbalanced number of healthy versus diseased tree plots due to sudden oak death progression, it may cause a bias in model training. We extracted various numbers of plots each year to balance the number of the two tree classes. We randomly allocated the photo interpretation-derived plots, but also created a buffer to avoid the neighborhood of field plots (100 m in size). The final reference dataset includes 40 diseased and 40 healthy tree plots every year during the 2005–2016 study window. We were aware of the positional errors in NAIP and Google Earth imagery (Potere, 2008; USDA, 2012). Because of the higher accuracy in NAIP data (6 m of true ground at a 95% confidence level, USDA, 2012), we relied more on NAIP to collect annual imagery (2005, 2009, 2010, 2013, 2014, and 2016), which were supplemented by Google Earth (2006, 2011, and 2015). We further compared our field plots (with GPS-measured accurate positions) with the targets identified on NAIP and Google Earth imagery. The errors were noticeably smaller than 30 m, which did not have a major effect on the modeling accuracy since our model was built at the 30 m resolution using Landsat data as the major input.

3.2. AVIRIS data

We collected AVIRIS (Airborne Visible/Infrared Imaging Spectrometer) data on September 24, 2008. AVIRIS is an airborne hyperspectral sensor developed and operated by NASA's Jet Propulsion Laboratory (JPL) flown on ER-2 and Twin Otter aircrafts mainly over the United States. The AVIRIS sensor consists of 224 contiguous spectral bands in the range of ~360 nm to ~2500 nm with an average bandwidth of 10 nm (Clark et al., 2002). The cloud-free AVIRIS spectral radiance image mosaic covered the northern part of our study area (27,925 ha), with a spatial resolution of 3 m. To mitigate the topographic effects in the mountainous regions, the topographic correction method recently developed by K.S. He et al. (2015) and T. He et al. (2015) was applied on the basis of slope and aspect provided along with the AVIRIS flight data, which was processed using a 30 m resolution digital elevation model (DEM) derived from the data collected by Advanced Spaceborne Thermal Emission and Reflection Radiometer (ASTER) as part of the Global Digital Elevation Model Version 2 (GDEM V2) project (ASTER GDEM Validation Team, 2011). Finally, the AVIRIS image mosaic was converted to surface reflectance bands using the 5th version of MODerate resolution atmospheric TRANsmission (MODTRAN5) as described by Berk et al. (2006).

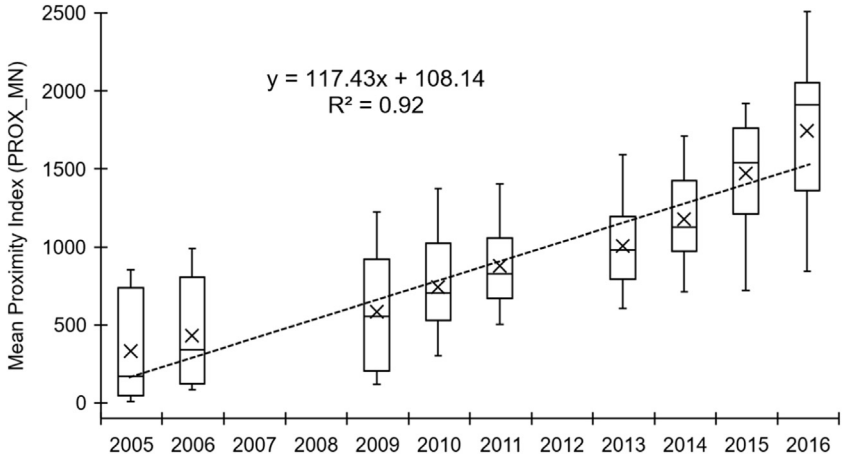

Fig. 4. Temporal trajectory of the mean proximity index (PROX_MN) for the dead trees affected by sudden oak death.

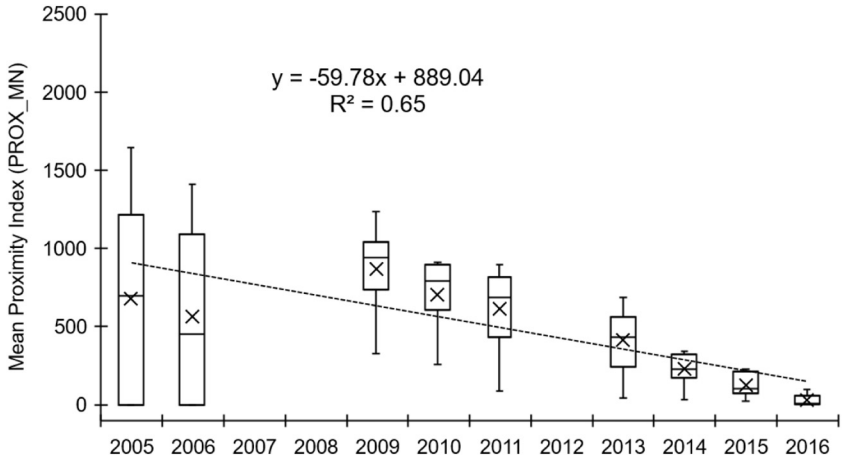

Fig. 5. Temporal trajectory of the mean proximity index (PROX_MN) for the dead trees not related to sudden oak death.

3.3. Landsat imagery

To retrieve the spatial and temporal patterns of sudden oak death progression annually from 2005 to 2016, we downloaded a total of eight Landsat-5 TM (Thematic Mapper) and five Landsat-8 OLI (Operational Land Imager) image scenes covering our study area (path: 43, row: 35) via the U.S. Geological Survey (USGS) Earth Resources Observation and Science (EROS) Center's Science Processing Architecture (ESPA) interface (https://espa.cr.usgs.gov). We did not use Landsat data from 2012, due to Landsat 5's mechanical failures and Landsat 7's Scan Line Corrector (SLC) failure. Although there are wavelength differences between sensors, we used the six bands that have been consistently acquired by all the sensors, including blue, green, red, NIR, SWIR-1, and SWIR-2 (NASA, 2018). All the images were acquired in the growing season (April–June, Table 1). Because some of the areas were covered by clouds in 2006 and 2013, we generated a cloud-free mosaic for each of the two years through compositing two image scenes acquired in the same month. During the process, cloud pixels were simply replaced by the cloud-free pixels of the same locations. Because the images used for merging were from the same months over the same region, we visually interpreted the images and found low spectral variation over the same ground objects between different dates. The high quality radiometric correction completed by USGS also ensured the minimized impact of our merging process. In our study, we directly used the Landsat Surface Reflectance level-2 science products, which have been geometrically, radiometrically, and topographically corrected by USGS before being made available online. Please refer to Landsat 4–7 Surface Reflectance Product Guide (USGS, 2018a) and Landsat 8 surface reflectance product guide (USGS, 2018b) for details about Landsat surface reflectance products.

3.4. NAIP imagery

NAIP (Airborne Visible/Infrared Imaging Spectrometer) imagery was acquired in 2005 at a 1.0 m resolution (a.k.a., ground sample distance - GSD) with a horizontal accuracy that matches within six meters of photo-identifiable ground control points. It was a three-band (Red, Green and Blue, or RGB) image mosaic with high quality data covering a portion of our study area. The data were downloaded from the U.S. Department of Agriculture (USDA) Farm Service Agency with free access (https://datagateway.nrcs.usda.gov/). The data were geometrically and radiometrically corrected by USDA.

3.5. Environmental variables

We used two groups of environmental variables known to affect the transmission of *P. ramorum* (Meentemeyer et al., 2008a): climate (i.e., precipitation, temperature, and relative humility) and topographical variables [i.e., elevation, slope, solar insolation index (SII), and topographic wetness index (TWI)] (Table 2). For climate, we calculated each variable using the monthly mean data during the disease's general reproductive season from December to May prior to each state transition over a period of 10 years (2007 to 2016). We selected this time period mainly due to the proven correlation between pathogen progressions with local climatic conditions (Meentemeyer et al., 2008a). This time period was selected in order to model the response of disease to annual patterns of climate, not individual weather events (Sturrock et al., 2011). The employed climate data were part of a broader-scale database Daymet (https://daymet.ornl.gov), at a 1 × 1 km resolution over the conterminous United States (Thornton et al., 2018). For topographical conditions, we calculated four variables from a 30 m resolution DEM, derived from the ASTER's GDEM V2 product, including elevation, slope, SII, and TWI. We calculated SII for each 30 m cell as the potential mean solar radiation in the rainy season using the cosine of illumination angle on slope equation (Dubayah, 1994). We further calculated TWI as the natural log of the ratio between the upslope contributing drainage area and the slope gradient of a grid cell to quantify topographic control on hydrological processes (Moore et al., 1991).

4. Methods

Our research framework has two major steps: (i) model development, and (ii) model application to multi-temporal disease distribution mapping. Generally, Step (i) was conducted for 2005, the beginning year of the studied time window 2005–2016 (see flowchart of step 1 in

Table 1
Acquired dates for time-series Landsat imagery.

	2005	2006	2007	2008	2009	2010	2011	2013	2014	2015	2016
April							4th	16th + 25th	28th	15th	17th
May		8th + 15th		13th	16th	3rd					
June	6th		12th								

Table 2
Description of the evaluated environmental factors.

Factor type	Factor name	Description
Climate	Precipitation	Monthly (December–May) mean precipitation of 10 years (2007 to 2016)
	Temperature	Monthly (December–May) mean maximum temperature of 10 years (2007 to 2016)
	RH	Monthly (December–May) mean relative humidity of 10 years (2007 to 2016)
Topography	Elevation	Elevation
	Slop	Slope
	TWI	Topographic wetness index
	SII	Solar insolation index

Fig. 6). To balance the needs for fine-scale monitoring of disease distribution and satisfactory coverage at broad scales, we applied spectral unmixing to extract sub-pixel disease presence in Landsat imagery, and derived an NPV (non-photosynthetic vegetation) fraction map to simulate tree mortality. The AVIRIS image mosaic was used to extract endmembers to facilitate spectral unmixing. We further developed a species distribution model and subsequently a probability map for assessing the probability of sudden oak death infection. We employed the 2005 reference data and the NAIP image of the same year to generate a high-resolution disease map for calibrating and validating the species distribution model. The probability map was compared with the reference disease presence/absence for determining a probability threshold, by which disease distribution was mapped for 2005. In Step (ii), an NPV fraction and a probability map were generated for each of the succeeding years (2006–2016). The annual disease-caused tree mortality maps were derived by applying the probability threshold (Step i) to all the probability and the corresponding year of NPV fraction maps. Fig. 6 shows the main components in model development and application. Please refer to the following subsections for detail and explanation. The annual disease-caused tree mortality maps were derived by applying the probability threshold (Step i) to all the probability and the corresponding year of NPV fraction maps. The accuracy of the tree mortality maps was individually evaluated using the annual reference data (see Section 3.1).

4.1. Spectral library extraction

We constructed a spectral library to include the spectra of four endmembers in our study area: green vegetation (GV), non-photosynthetic vegetation (NPV), soil, and shade. We intended to use GV to represent healthy trees. Here, we tried to build an NPV spectral library biased to sudden oak death, although we expected an overestimation of NPV-derived diseased trees because other disturbances (e.g., drought) may have resulted in similar spectra. Due to no pre-existing library including the spectral signatures from sudden oak death-impacted forests, we extracted image endmembers from the hyperspectral AVIRIS data acquired over the same region. Compared to field radiometry surveys, such method was cost-effective, allowing us to efficiently collect a large number of reflectance values associated with disease infection. Using the AVIRIS data, we applied the Pixel Purity Index (PPI) algorithm to identify a large number of potential endmember pixels with unique spectral signatures. The classic PPI is an iterative process, in which every pixel is repeatedly projected onto a random vector selected through the n-dimensional scatter plot (n = 224 in our study); and pixels are considered pure if they constantly fall into the tails of the calculated histograms. The threshold for defining histogram tails affected the number of the endmember pixels identified by PPI. After an initial assessment, we used the threshold value 5 to extract 200 endmember candidate pixels.

To select the most appropriate endmembers for our study, we first applied sub-meter Google Earth WorldView-1 images (observation dates in the similar time window as that of AVIRIS data acquisition) as a reference to reduce the number of endmember pixels to 47: 17 (GV), 13 (NPV), 14 (soil), and 3 (shade). To further refine the result, we used the following three metrics.

1) Endmember Average RMSE (root mean squared error) (EAR): EAR was used to select the most representative endmember for each land cover class. It was calculated for each endmember by averaging the RMSE of the set of models that used the endmember to unmix the spectra belonging to the same land cover class (Roberts et al., 2003).

$$\mathrm{EAR}_i = \frac{\sum_{j=1}^{N} \mathrm{RMSE}_{i,j}}{n-1} \tag{2}$$

where i is an endmember, j is the modeled spectrum, N is the number of endmembers, and n is the number of modeled spectrum. The term n-1 corrected for a zero RMSE resulting from an endmember itself. EAR was used to evaluate the ability of each endmember to model the spectra within its own class. Endmembers possessing a lower EAR model spectrum within their land cover class were better than endmembers with a higher EAR. The minimum EAR endmember should be the most representative of its modeled class.

2) Minimum Average Spectral Angle (MASA): MASA within a class was calculated as the average spectral angle between the reference spectrum (candidate model) and all other spectra within the same class. The best MASA candidate was selected as the one that produced the lowest average spectral angle (Dennison et al., 2004).

$$\mathrm{MASA}_i = \frac{\sum_{j=1}^{N} \theta_{i,j}}{n-1} \tag{3}$$

$$\theta = \cos^{-1} \frac{\sum_{\lambda=1}^{M} \rho_\lambda \rho'_\lambda}{L_\rho L_{\rho'}} \tag{4}$$

$$L_{\rho'} = \sqrt{\sum_{\lambda=1}^{M} \rho_\lambda^2} \tag{5}$$

where ρ_λ is the reflectance of an endmember, ρ_λ' is the reflectance of a modeled spectrum, L_ρ is the length of the endmember vector, and $L_{\rho'}$ is the length of the modeled spectrum vector. MASA was similar to EAR in that it was designed to select spectra with the best average fit within a class, while differing from EAR in that the measure of fit used was the spectra angle instead of RMSE.

3) Count-based Endmember Selection (CoB): CoB was used to select optimal endmembers as those members of a library that modeled the greatest number of spectra within their class, while assessing whether these candidate models met fraction, RMSE and residual constraints when unmixing any other spectrum in the library (Roberts et al., 2003). CoB used the MESMA concept to select endmembers based on the number of library spectra, determining the number of spectra modeled by an endmember within the endmember's class (InCoB) and outside of endmember's class (OutCoB). The optimum model had the highest InCoB and lowest OutCoB.

The processing used the tool – Visualization and Image Processing for Environmental Research (VIPER; Roberts et al., 2007), which generated the final spectral library (including 6 spectra for GV, 5 spectra for NPV, 6 spectra for soil, and 1 spectrum for shade) and the corresponding fractions.

4.2. MESMA procedure

Using the constructed spectral library, we applied spectral unmixing to decompose each of the Landsat pixels acquired in 2005 into three components: GV, NPV, and soil. Spectral unmixing was implemented by

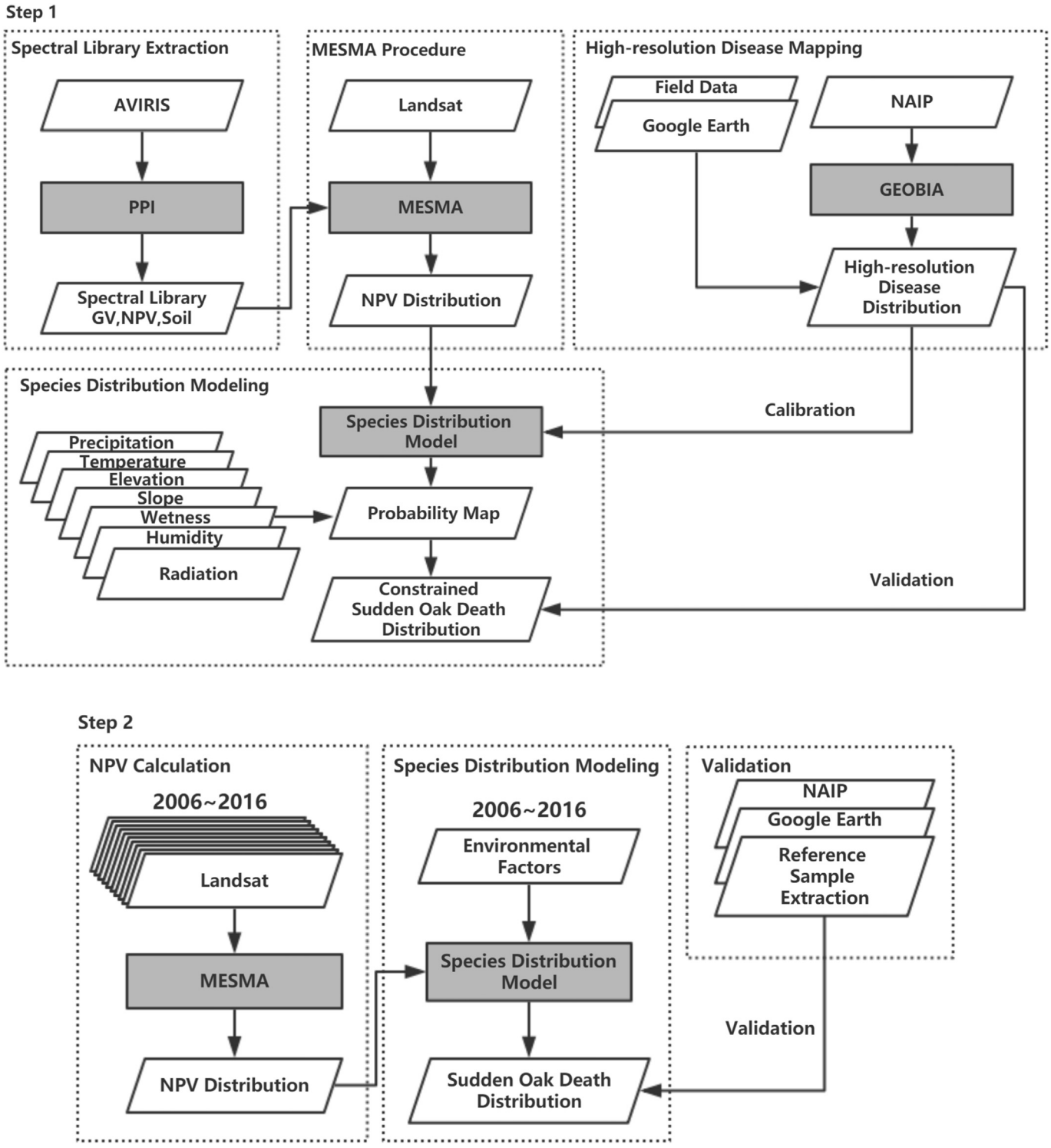

Fig. 6. Detailed working flow for model development (Step1) and annual disease-caused tree mortality mapping (Step 2).

Table 3
A confusion matrix to evaluate the result of a presence-absence (binary) model.

User class	Reference class	
	Presence	Absence
Presence	True Positive (TP)	False Positive (FP)
Absence	False Negative (FN)	True Negative (TN)

the classic Multiple Endmember Spectral Mixture Analysis (MESMA) algorithm, which considers spectral variability allowing the number and type of endmembers to vary on a per-pixel basis (Roberts et al., 1998). The criteria used to determine the best-fit models included endmember fractions, maximum shade fraction, and RMSE. We chose the following thresholds: −0.05 and 1.05 for minimum and maximum allowable fraction values, respectively; 0.8 for maximum allowable shade fraction value; and 0.025 for maximum allowable RMSE. Those thresholds were initially determined from the literature (Roberts et al.,

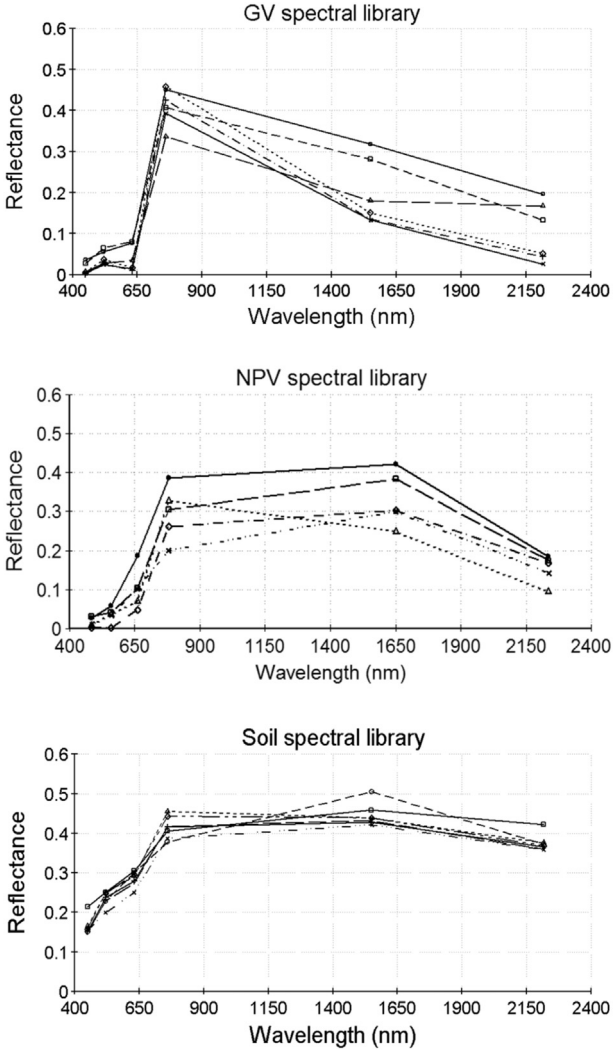

Fig. 7. The extracted spectra for green vegetation (GV), non-photosynthetic vegetation (NPV), and soil in our study area.

1998), and adjusted through our tests, in which we evaluated all the reasonable endmember combinations and selected the best-fit model. When multiple models met these criteria, the model with the lowest RMSE was chosen. Finally, shade normalization was performed to remove shade fraction, redistributing this fraction proportionally among all other non-shade endmembers (Roberts et al., 2007). We employed the VIPER package to complete the MESMA procedures (Roberts et al., 2007). Given the fact that our study focused on forests, we excluded the soil, and shrub/grass components from all NPV images (2005–2016) using the 2005 NAIP-derived classification result (see Section 4.3).

4.3. High-resolution disease mapping

We generated a high-resolution disease distribution map for 2005, the beginning year of the study time window. The map was for SDM calibration and validation (Section 4.4), mainly because the accuracy of SDM depends on the number and quality of species reference samples (Carneiro et al., 2016). In our study, field-measured data were limited, which may not provide a reliable knowledge of sudden oak death distribution. Here, we integrated the 1.0 m resolution NAIP image mosaic and the reference data acquired in 2005 to generate a high-resolution tree mortality map. This map was later used to extract a large number of samples of sudden oak death distribution for reliable SDM calibration and validation (Section 4.4).

To generate the map, we applied a geographic object-based Image Analysis (GEOBIA) framework following Chen et al. (2012). Compared to the classic pixel-based approach, GEOBIA uses image-objects (i.e., pixel clusters) as the basic study units to reduce errors caused by spectral variation within each geographic object (e.g., individual trees containing sunlit and shaded crowns; Chen et al., 2015a). Our framework has two components: image segmentation and object-based classification, both of which were completed in the eCognition Developer 9.0 environment (Trimble, Sunnyvale, USA).

Image segmentation was conducted on the NAIP image mosaic using the eCognition's classic multiresolution segmentation algorithm. A crucial issue involved in segmentation is defining an appropriate Mean Object Size (MOS), or spatial scale of analysis. A large MOS may cause under-segmentation where an image-object contains more than one land-cover class. However, a very small MOS may introduce biases where an image-object may only contain sunlit or shaded canopies resulting from the complex sun-tree-sensor geometry. We followed the recommendations by Chen et al. (2017), and the value 30 for MOS was chosen to accurately capture relatively small, homogenous land-cover patches, where the majority of trees within image-objects were either dead or healthy. In addition to MOS, the default value of 0.1 was used for the shape parameter, while the compactness parameter was set at 0.8 to obtain relatively smooth forest object boundaries.

Object-based classification used the segmentation-derived image-objects, instead of pixels, as the basic mapping units. To extract spectral features for classification, we followed Chen et al. (2017), who successfully used three groups of features – spectral (mean), texture (standard deviation), and geometry (compactness, length/width ratio, roundness, and shape index) – to map sudden oak death-caused tree mortality. Compared to many other causes of mortality, sudden oak death has resulted in uniquely spatial and spectral appearances in tree crowns (Section 3.1). We expected to use these features to capture the unique traits of diseased trees. Here, we categorized the image into three classes: (i) healthy forest, (ii) diseased forest, and (iii) others. This step was accomplished by applying the eCognition's nearest neighbor algorithm, a supervised classification approach. Half of the 2005 reference samples for each land-cover class were used for training, while the remaining samples in the same year were applied for validation.

4.4. Species distribution modeling (SDM)

We developed a generalized linear model (GLM) to analyze the degree to which ecological conditions influenced the probability of sudden oak death infection. GLM is an extension of ordinary multiple regression that allows for modeling non-normal response variables, which has been used for modeling disease risks (e.g. Meentemeyer et al., 2008a). Here, we modeled the infection probability of sudden oak death as a function of seven environmental variables (i.e., precipitation, relative humidity, temperature, elevation, slope, SII, and TMI) by following the recommendations of Meentemeyer et al. (2008a, 2008b), who studied sudden oak death in the same region. We used the logit link function in GLM, which is synonymous with logistic regression employing a maximum likelihood parameter optimization technique to model the log odds of a binary response variable (Franklin, 1995). The logit transformation of the probability (p_i) that a susceptible plot i (equivalent of the area of a Landsat pixel) becomes invaded is described as:

$$Y_{\text{infection}} = \text{logit}(p_i) = \log \frac{p_i}{1 - p_i} = \beta_0 + \sum_{j=1}^{8} \beta_j x_j \quad (6)$$

where β_0 and β_i are the regression coefficients, and x_j is one of the eight environmental variables. Meentemeyer et al. (2008a) discovered a rapid decline of *P. ramorum* invasion probability as the distance to the previous year of infection (i.e., sources of inoculum) increases. Particularly when the distance is longer than 1 km, the probability that a

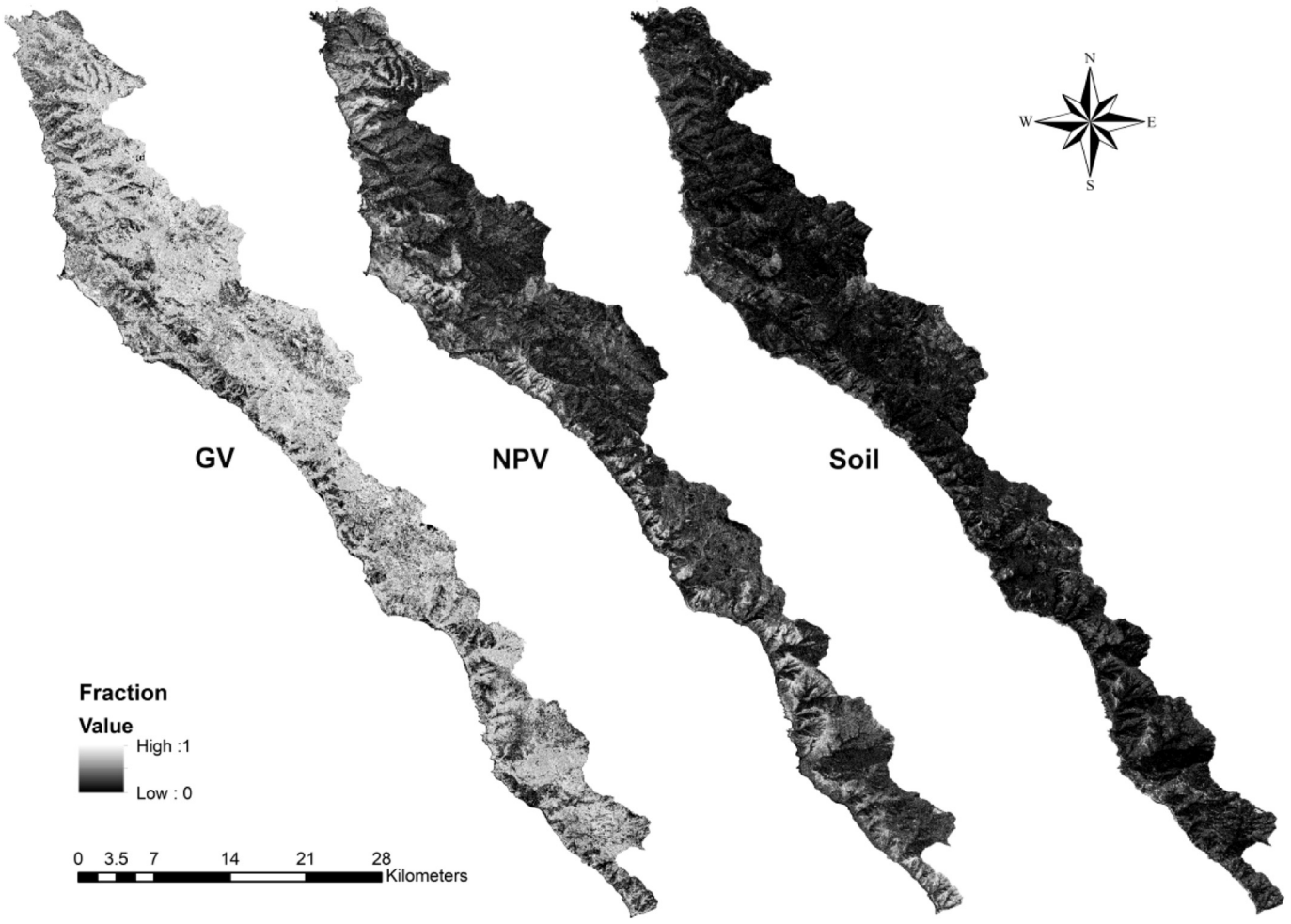

Fig. 8. Fraction maps of green vegetation (GV), non-photosynthetic vegetation (NPV), and soil for year 2005, where gray tones represent values from low (black) to high (light).

Table 4
Confusion matrix for the disease mapping result.

User class	Reference class				
	Healthy forest	Diseased forest	Others	Total	Producer's accuracy (%)
Healthy forest	35	4	1	40	87.50
Diseased forest	3	34	2	39	87.17
Others	2	2	37	41	90.25
Total	40	40	40	120	
User's accuracy (%)	87.50	85.00	92.50		

Overall accuracy = 88.33%; Kappa statistic = 0.82.

susceptible plot may be invaded is very low. In this study, we applied a fixed dispersal kernel (1 km in Euclidean distance) to constrain the maximum infection distance for each year.

To reduce multicollinearity among the independent variables, the Pearson's linear correlation coefficients were calculated for all the variables. Then, we applied the variable reduction method as described in Chen et al. (2015b). That is, each independent variable was evaluated and retained under two rules: (1) its correlation with any other independent variable should be lower than 0.7; or (2) if its correlation with another one or several independent variables is higher than 0.7, the variable should have the highest correlation value with the dependent variable. After discarding redundant independent environmental variables/factors, we applied regression analysis and assessed model's adjusted R^2, RMSE (root mean square error) and AIC (Akaike information criterion) values in the statistical environment R package (R Core Team, 2017, Vienna, Austria). For model calibration, we extracted 300 sample points (150 diseased and 150 healthy samples to ensure a balanced representation of trees affected and not affected by sudden oak death) from the previously generated high-resolution tree mortality map (Section 4.3). We used a stratified random sampling strategy to collect samples from diseased and healthy tree classes, respectively. To ensure the quality of the samples, we manually checked all the samples following the same image interpretation approach as described in the reference data section (Section 3.1). If the sample did not appear to be affected by the disease, we selected a new sample in its neighborhood.

We further compared the probability derived from the SDM (Eq. (6)) with the NPV fraction (Section 4.2) at the sample locations. We used the reference disease presence/absence data to determine the best probability threshold, with results reaching the maximum kappa statistic value (Freeman and Moisen, 2008), i.e., a Landsat pixel area was deemed to be affected by sudden oak death if its probability value was higher than the threshold. We also applied the reference data to conduct an accuracy assessment using confusion matrix to calculate True Skill Statistic (TSS), a measure reflecting true ecological phenomena in presence-absence models (Allouche et al., 2006). Specifically, for the binary classification, the confusion matrix records the number of True Positive (TP), False Positive (FP), False Negative (FN) and True Negative (TN) cases predicted by the model (Table 3). Sensitivity is the probability that the model correctly classifies a presence (Eq. (7)).

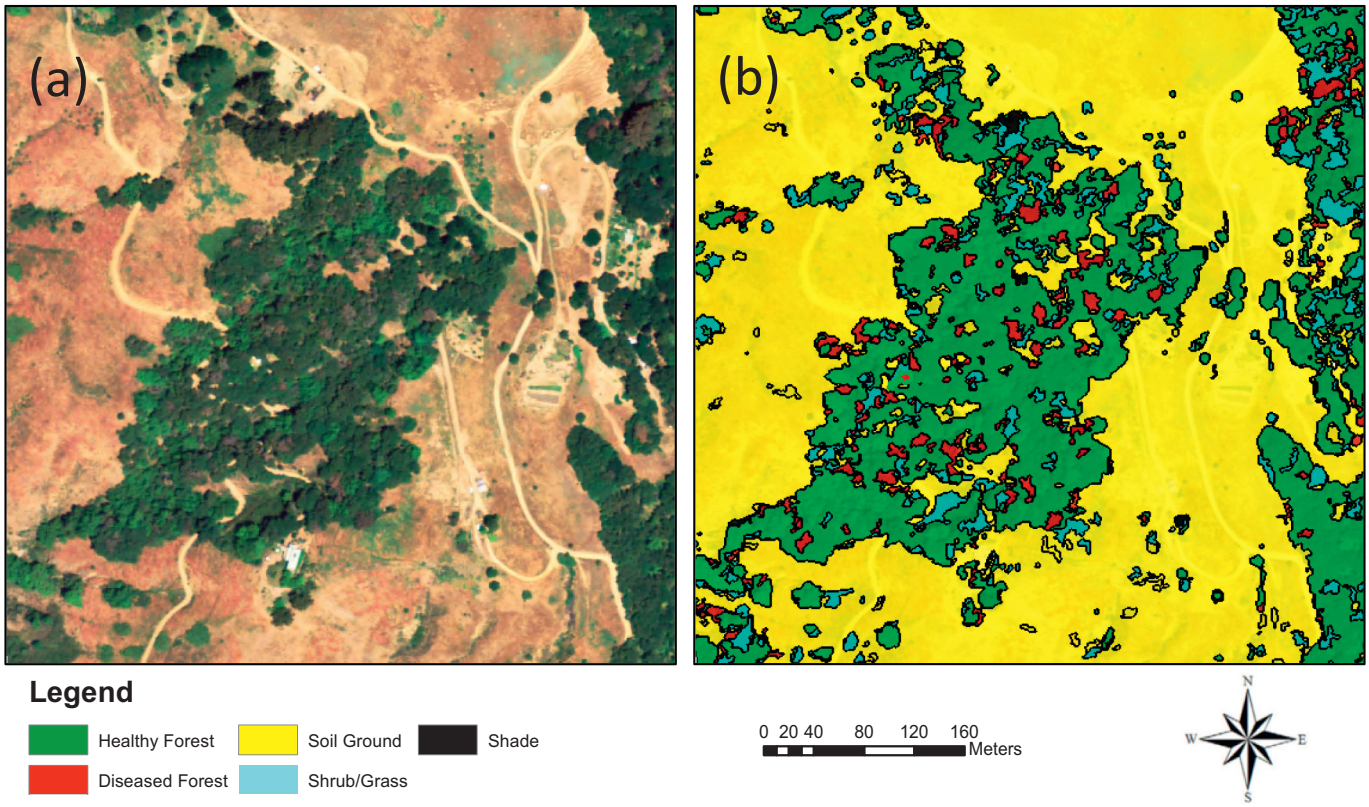

Fig. 9. (a) True color sample NAIP image in the Big Sur, CA study region, and (b) corresponding classification with image-object boundaries. (For interpretation of the references to color in this figure legend, the reader is referred to the web version of this article.)

Specificity is the probability that the model correctly classifies an absence (Eq. (8)). TSS equals the difference between the sum of sensitivity and specificity and constant one (Eq. (9)).

$$\text{Sensitivity} = \frac{TP}{TP + FN} \tag{7}$$

$$\text{Specificity} = \frac{TN}{FP + TN} \tag{8}$$

$$TSS = \frac{TP}{TP + FN} + \frac{TN}{FP + TN} - 1 \tag{9}$$

4.5. Annual disease-caused tree mortality mapping

We applied the spectral unmixing MESMA model to each of the Landsat images from 2006 to 2016, which produced annual NPV fraction maps. Meanwhile, the SDM was employed to produce yearly probability maps of sudden oak death infection (see Step 2 in Fig. 6). We overlapped the two types of maps of the corresponding year. The probability threshold (Section 4.4) was used to determine whether an NPV-identified pixel was affected by sudden oak death or not. We considered that a 30-m pixel area is affected by the disease if a disease reference sample is found in the area. This is based on the nature of SDM, which only considers infection and non-infection for each pixel area. Consequently, a total of 10 maps were produced to show annual sudden oak death progression from 2006 to 2016. The final mapped results were assessed using the reference data that were collected annually (see Section 3.1), with confusion matrices, coverall accuracies, and kappa statistics calculated for accuracy assessment.

5. Results

5.1. Endmembers and fraction images

The spectral reflectance for the extracted 6 GV, 5 NPV and 6 soil endmembers are presented in Fig. 7. Overall, the GV endmembers revealed higher intra-class variation than the NPV and soil endmembers. This was mainly because trees in the study area were comprised of a variety of species types, including mixed oak woodlands and coniferous forests. Compared to healthy trees, dead trees and soil were relatively homogeneous in terms of spectral signatures. Especially for the dead trees, their spectral reflectance values were extremely low in the near infrared portion of the spectrum (760–900 nm) and high in the shortwave infrared portion (1550–1750 nm), making NPV distinguishable from GV and soil. Uncertainties occurred mainly between some GV and soil endmembers. There were barren lands in the study area, although forest floor was often made up of soil, decaying logs/leaves and grass/shrubs.

The fraction maps corresponding to the three components of GV, NPV and soil for year 2005 are shown in Fig. 8. Live trees covered much of the study in 2005, as evidenced by the high GV fraction values. High NPV values mainly occurred on the west coast, which is consistent with findings by Meentemeyer et al. (2008b), who used 0.33 m resolution aerial photos to manually digitize sudden oak death-caused tree mortality over the same area.

5.2. Fine-resolution tree mortality map

The overall accuracy of the classification result using the 2005 NAIP imagery and the object-based framework was 88.33%, with a Kappa statistic of 0.82. As presented in Table 4, others achieved better performance. Compared to the non-forest landscapes, forest horizontal and vertical structure was of higher complexity and heterogeneity, resulting

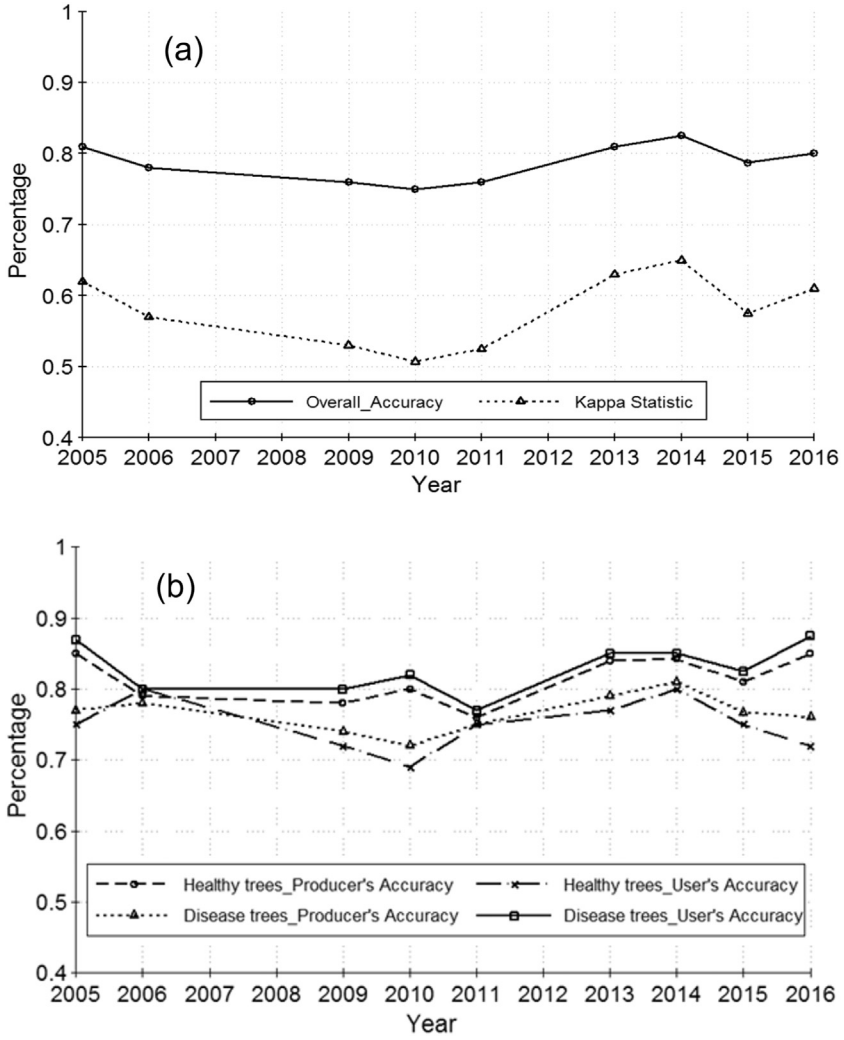

Fig. 10. Mapping accuracies (producer accuracy, user accuracy, overall accuracy, and Kappa statistic) in years 2005, 2006, 2009, 2010, 2011, 2013, 2014, 2015 and 2016. See methods of accuracy assessment in Section 4.5.

in a higher spectral variation. Compared to the healthy forests, diseased forests were more difficult to map showing relatively lower user's and producer's accuracies (Table 4). Uncertainties mainly occurred in the land-cover transitional zones, where dead trees were interspersed with their healthy counterparts or soil. Because sudden oak death had a non-random, highly-localized distribution pattern (Meentemeyer et al., 2011), some small patches of diseased trees were closely surrounded by healthy forests [see (a) in Fig. 9]. In addition, trees affected by the disease changed colors progressively over years, which made it difficult to accurately extract all the diseased trees. For example, some may be at the non-visible early stage of infection. In the transitional zones, we also observed a mixture of soil, and sparsely distributed vegetation within single image-objects [see (b) in Fig. 9]. The averaged reflectance from those objects was similar to that of a diseased forest object (Chen et al., 2017). Although the mapping was challenged by a small portion of transitional zones, the extracted 300 samples (Section 4.3) were all manually checked to ensure the quality for reliable SDM calibration and validation.

5.3. Species distribution modeling (SDM)

Three environmental variables were selected in the SDM, including precipitation, temperature, and elevation (Eq. (6)). These variables together explained 36% of the variation (adjusted R^2: 0.36) of the probability of sudden oak death infection. The TSS value 0.78 for our SDM was considered satisfactory following the suggestion by Shirk et al. (2018), in which multiple SDM types (including ours) were comprehensively compared for modeling the spread of white pine blister rust in the Western U.S. Their acceptable TSS values were located in the range between 0.71 and 0.84. We found increased probability with the increase of maximum temperature, and precipitation; however, probability was negatively correlated with elevation. Our findings of significant variables are similar to those in an earlier study, where 2003–2005 field measurements were used in species distribution modeling for predicting the probability of sudden oak death invasion (Meentemeyer et al., 2008a; Meentemeyer et al., 2008b). Using calibration data further allowed us to determine the best probability threshold 0.62. Hence, a Landsat pixel was deemed sudden oak death-impacted if its probability value was equal to or higher than 0.62.

$$Y_{\text{Infection}} = -8.4606 + 0.0434 \times \text{Precipitation} + 0.3290 \times \text{Temperature} - 0.0046 \times \text{Elevation} \quad (10)$$

5.4. Annual maps of disease-caused tree mortality

Following the application of the proposed mapping method, the long-term sudden oak death-caused tree mortality maps achieved overall accuracies between 0.7 and 0.9, with Kappa statistics ranging

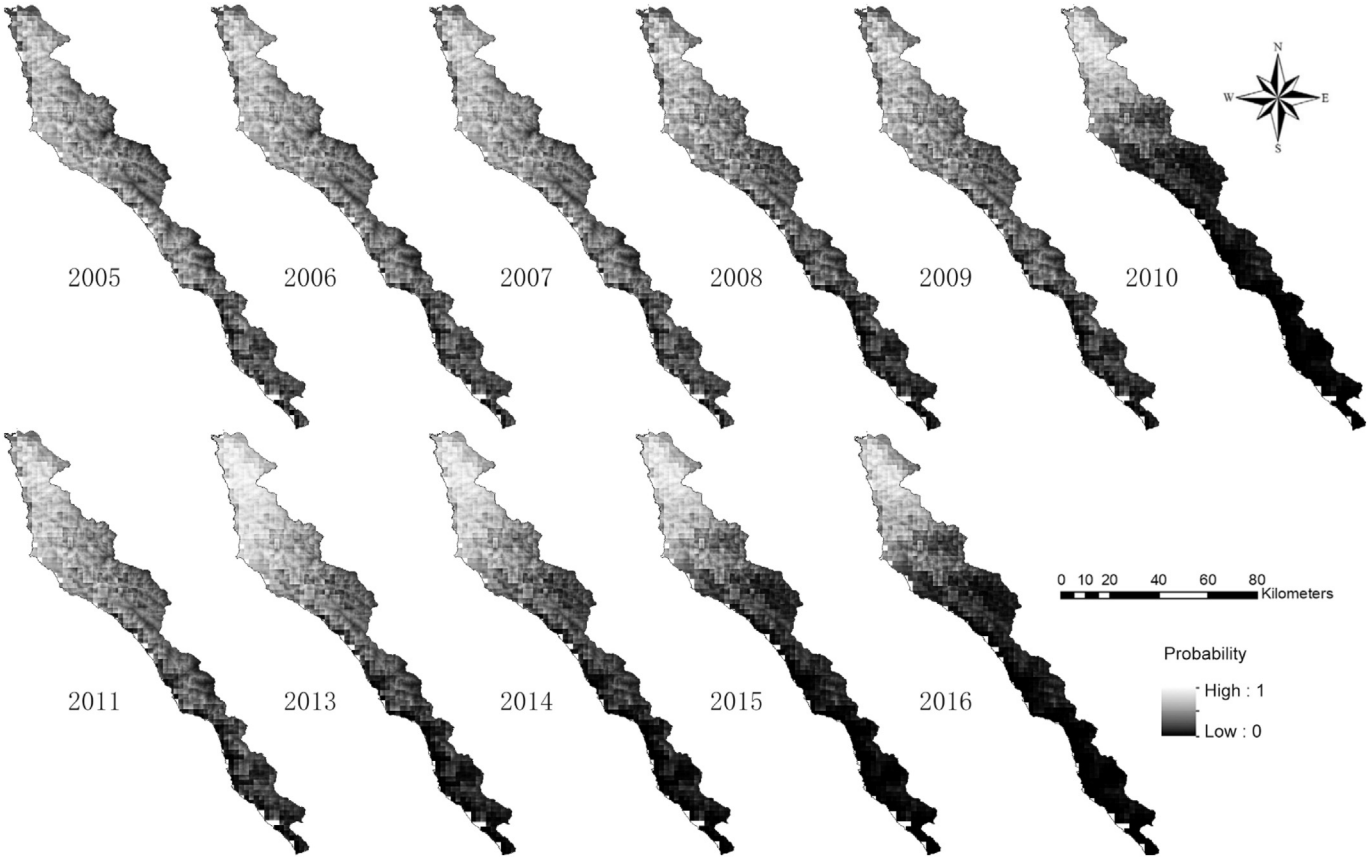

Fig. 11. Species distribution model derived probability map of sudden oak death infection from 2005 to 2016.

from ~0.5 to ~0.7 [see (a) in Fig. 10]. The mapping accuracies for years 2005, 2013, 2014, and 2016 were higher than 80%, while relatively inferior performance (75%–80%) was obtained in years 2006, 2009, 2010, 2011 and 2015 [see (a) in Fig. 10].

We applied the developed SDM to the entire study area and generated a probability map of sudden oak death infection (Fig. 11). When it was overlaid with field plots, we found that potential habitat suitability with high probability was significantly greater ($p < 0.05$) in the invaded plots. All the 11 tree mortality maps (2015–2016) are included in Fig. 12, which shows annual sudden oak death infection in the study area. Those maps illustrate a spatial progression pattern of disease mainly from the west coast to the northeast. The spatial coverage of sudden oak death-caused tree mortality rose rapidly from 1584 ha in 2005 to 3178 ha in 2016, a 2-time increase over a decade, at an annual infection rate of 7%. Such an aggressive progression pattern is consistent with the field findings discussed in the literature (e.g., Rizzo et al., 2005; Cunniffe et al., 2016).

6. Discussion

6.1. Assessment of disease mapping using spectral unmixing

While plant disease-caused tree mortality has reached epidemic levels in forest landscapes, such as California's coastal forests (Chen and Meentemeyer, 2016), many diseases (including sudden oak death) demonstrate isolated, patchy progression patterns. In our study, spectral unmixing proved to be effective for extracting tree mortality at the Landsat sub-pixel level. Such an approach differs from the previous efforts of sudden oak death modeling, which solely relied on high-spatial resolution imagery for small-area mapping (e.g., Kelly et al., 2007; Liu et al., 2006; Meentemeyer et al., 2008a). Through comparing MESMA-derived NPV fractions (Fig. 8) with the high-resolution sudden oak death map, we found a similar pattern of disease occurrence mainly on the west coast of the study area in 2005.

Although promising, spectral unmixing was found to overestimate disease-caused tree mortality. For example, Fig. 8 shows high-value NPV pixels in some of the southern and eastern parts of the region, which have yet to be heavily impacted by sudden oak death in 2005 according to field observations and high-spatial resolution images. Similar overestimation patterns were found in the NPV results over the succeeding years. This was mainly due to the use of Landsat imagery that has a limited number of spectral bands, unable to accurately identify the spectral differences in some dead trees affected by sudden oak death versus other disturbances (e.g., extreme drought and wildfires). We also found relatively higher accuracies in the maps using the data collected more recently (e.g., years 2013, 2014, 2015 and 2016). Those data were from the Landsat-8 OLI sensor (as compared to the other data from Landsat 5 TM). The data quality (signal to noise ratio) and radiometric quantization (12 bits) of Landsat 8 OLI is higher than those of previous Landsat instruments (e.g., 8 bits for TM), providing a significant improvement in the ability to detect land cover on the Earth's surface (Roy et al., 2014). The improved data quality of Landsat 8 OLI may have positively contributed to such phenomenon. When comparing the mapping accuracies between healthy and diseased trees, the results showed differences [see (b) in Fig. 10]. From 2005 to 2016, the producer's accuracies of healthy trees were consistently higher than that of diseased trees, and their user's accuracies were lower [see (b) in Fig. 10].

6.2. Effects of SDM on disease mapping

The developed SDM indicated that higher probabilities were correlated with the forests experiencing relatively warm and wet climatic conditions, and that were located at low elevations in the mountainous

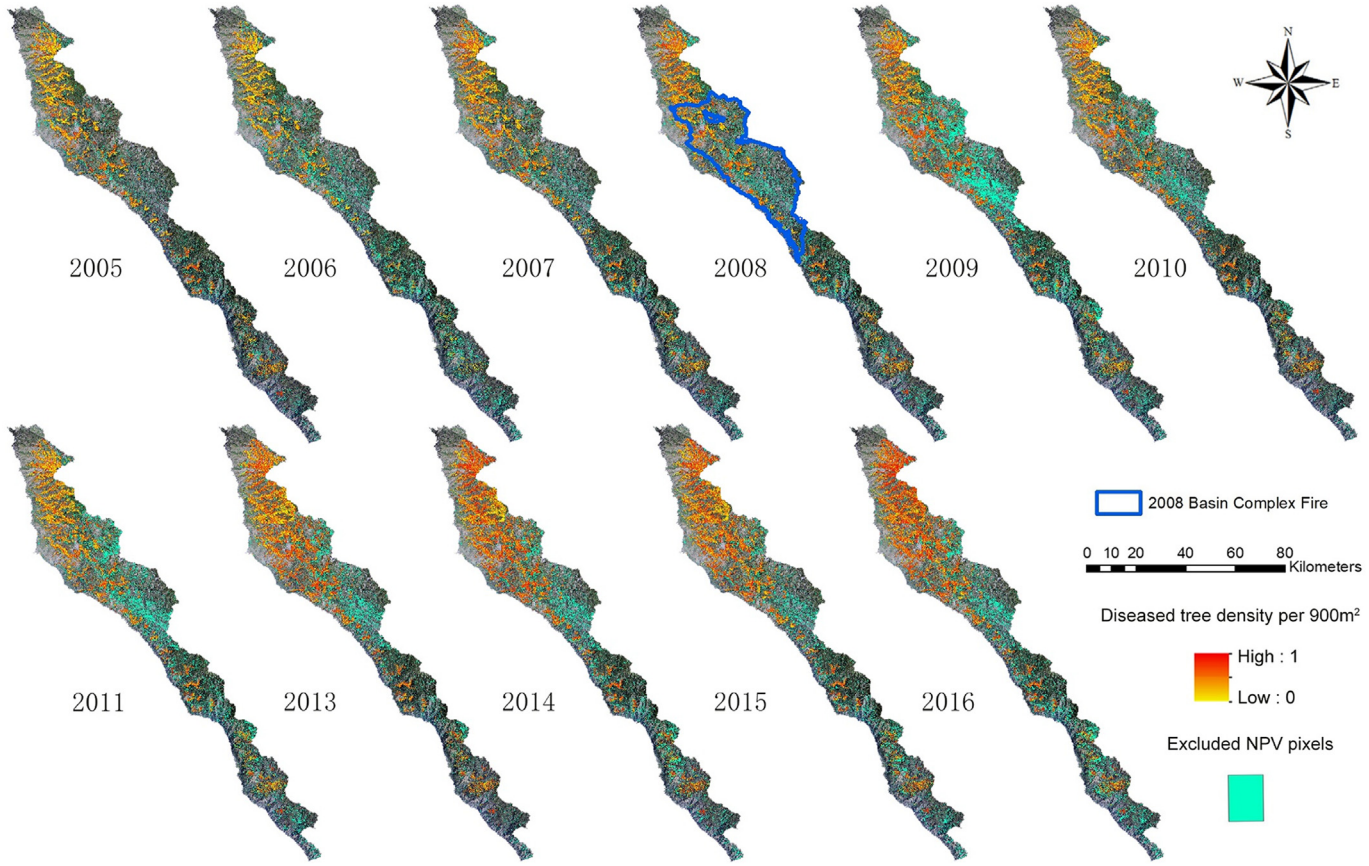

Fig. 12. Spatial distribution of the estimated density of sudden oak death-caused tree mortality per 900 m^2 from 2005 to 2016.

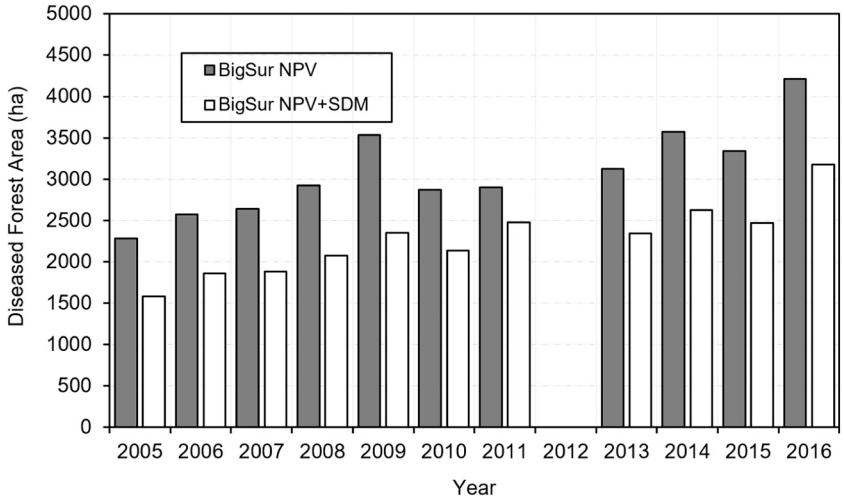

Fig. 13. Annual sudden oak death-impacted forest area from NPV versus NPV + SDM (species distribution model) for the entire study area.

study area (Eq. (10)). Similar significant factors (e.g., precipitation, temperature, and elevation) were found in a previous study by Meentemeyer et al. (2008a), who applied a SDM to predict the invasion of sudden oak death pathogen *P. ramorum* using field plots only.

Compared to the MESMA-derived NPV results, the SDM consistently improved the estimation of sudden oak death-caused tree mortality over years (see Fig. 13 for a comparison), leading to an average of 26% decrease in detecting diseased forests. This was equivalent to an average of 818.4 ha each year, ranging from the minimum of 424.8 ha and the maximum of 1187.1 ha. The difference between the NPV and the SDM-constrained results was partially explained by two major drought events that severely affected California's coastal ecosystems. For example, the overall rainfall levels in the central coast were about 50% of average over 2007–2009 (California Dept. Water Resources, 2010). Starting from 2012, the region experienced severe drought again for five consecutive years (U.S. Geological Survey, 2017). Our field visits and aerial photo interpretation both discovered large areas of stressed and dead tree canopies in the areas unsuitable to be infected by sudden oak death.

In summer 2008, the Basin Complex Fire that was ignited by a dry lightning storm burned the northern part of our study area (Fig. 12). Because some diseased trees revealed similar spectral reflectance as the

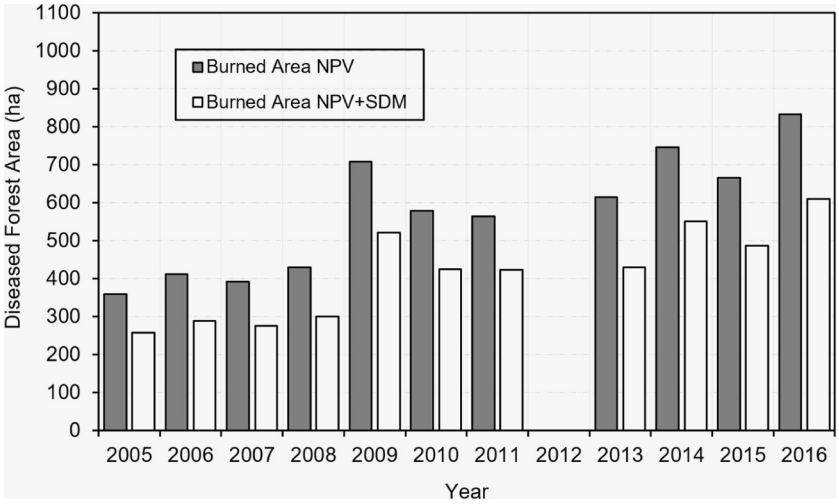

Fig. 14. Annual sudden oak death-impacted forest area from NPV versus NPV + SDM (species distribution model) in part of the study area that was burned in 2008 (see Fig. 12 for the location and size of the burned area).

burned trees owing to reduced foliage water content and damaged tree structure (Chen et al., 2017; He et al., 2019), the high spectral similarity and the relatively low Landsat spectral resolution did not provide sufficient information for MESMA to accurately extract diseased trees. Instead, MESMA treated some burned trees as being affected by sudden oak death, causing a major increase in the NPV result in 2009 (Fig. 14). In contrast, the SDM was able to mitigate the overestimation effect, making it valuable for generating reasonable sudden oak death progression maps in the regions affected by compound disturbances. However, the high-spectral similarities between burned (within five years following the fire occurrence) and diseased canopies definitely affect the effectiveness of SDM. Spectral similarities also apply to the drought- and disease-killed trees, although studies have found less severe tree mortality caused by drought in coastal forests (including our study area) than their inland counterparts (Baguskas et al., 2014; Fischer et al., 2009). Nevertheless, it is possible that the presence of sudden oak death remains overestimated by our model. Acquiring detailed field measurements of tree mortality caused by both the disease and fire/drought offers a solution to better train our model and assess its performance in distinguishing between the two disturbance types. Another viable solution, as suggested by He et al. (2019), is using hyperspectral data with enhanced spectral signatures from the shortwave infrared portion of the spectrum. Because different types of disturbances may reveal varying progression patterns over time, high-resolution time series images have the potential to capture those patterns. However, data acquisition and processing costs are considerably higher than using time series data at the medium resolution.

7. Conclusion

We developed a new mapping method to capture the spatiotemporal patterns of diseased-caused tree mortality in a forested area for over a decade. The rationale of integrating remote sensing and SDM was based on the fact that remotely observed tree mortality may be associated with both disease and non-disease disturbances; such uncertainties can be reduced by understanding pathogen spatial preferences for certain habitat conditions (i.e., using SDM). The proposed method bridges remote sensing and ecological SDM in a way that has not been well studied. Here, we used sudden oak death (caused by pathogen *P. ramorum*) as a case study of a rapidly spreading EID. The results show that SDM considerably reduced the overestimation of sudden oak death-caused tree mortality observable from Landsat imagery. However, due to the lack of detailed field observations (e.g., drought-caused tree mortality), we were unable to assess what percentage of the overestimation was from what specific causes, other than sudden oak death. Our interpretation that the overestimated tree mortality was mainly linked to drought/fire was based on the reported severe weather events in the region (Asner et al., 2016). Nevertheless, our study represents the best way linking multi-scale remote sensing observations to highlight areas that are probably not affected by sudden oak death so we can focus the disease management efforts in areas that need them. The final annual tree mortality maps show accuracies ranging from 75.5% to 82.5%. To balance data costs and the ability to map the pathogen's isolated, patchy distribution patterns, in this study we applied spectral unmixing to Landsat TM/OLI time series. Our model was calibrated and validated by disease reference data from high-resolution image samples (aerial NAIP and AVIRIS photos and Google Earth imagery) and field surveys. Coupling multi-sensor, multi-scale remote sensing (full-cover Landsat imagery and sampled high-resolution images) and SDM offers a timely and cost-effective means to map long-term forest disease progression at the regional scale.

Acknowledgement

This research was supported by the National Science Foundation (EF-0622770) as part of the joint NSF-NIH Ecology and Evolution of Infectious Disease program, the North Carolina Space Grant, and the University of North Carolina at Charlotte CLAS Junior Faculty Development Award. The authors also gratefully acknowledge financial support from the USDA Forest Service – Pacific Southwest Research Station, and the Gordon and Betty Moore Foundation. We thank numerous contributors who provided vital field and laboratory support, including J. Geng, K. Aram, M. Beh, A. Brauer, M. Chan, C, DeLong, W. Dillon, K. Frangioso, A. Hohl, H. Mehl, A. Oguchi, E. Paddock, K. Pietrzak, M. Vaclavikova, J. Vieregge, L. Waks and A. Wickland.

References

Alexander, J., 2012. The past, present, and future of sudden oak death. Outlooks on Pest Manag. 23, 72–76.
Allouche, O., Tsoar, A., Kadmon, R., 2006. Assessing the accuracy of species distribution models: prevalence, kappa and the true skill statistic (TSS). J. Appl. Ecol. 43, 1223–1232.
Anderegg, W.R.L., Kane, J.M., Anderegg, L.D.L., 2013. Consequences of widespread tree mortality triggered by drought and temperature stress. Nat. Clim. Chang. 3, 30–36.
Asner, G.P., 2013. Geography of forest disturbance. Proc. Natl. Acad. Sci. 110, 3711–3712.
Asner, G.P., Brodrick, P.G., Anderson, C.B., Vaughn, N., Knapp, D.E., Martin, R.E., 2016. Progressive forest canopy water loss during the 2012–2015 California drought. Proc. Natl. Acad. Sci. 113, 249–255.
ASTER GDEM Validation Team, 2011. ASTER Global Digital Elevation Model Version 2 –

Summary of Validation Results. Available online at. http://www.jspacesystems.or.jp/ersdac/GDEM/ver2Validation/Summary_GDEM2_validion_report_final.pdf, Accessed date: 20 March 2019.
Baguskas, S.A., Peterson, S.H., Bookhagen, B., Still, C.J., 2014. Evaluating spatial patterns of drought-induced tree mortality in a coastal California pine forest. For. Ecol. Manag. 315, 43–53.
Berk, A., Anderson, G.P., Acharya, P.K., Bernstein, L.S., Muratov, L., Lee, J., Fox, M., Adler-Golden, S.M., Chetwynd Jr., J.H., Hoke, M.L., Lockwood, R.B., Gardner, J.A., Cooley, T.W., Borel, C.C., Lewis, P.E., Shettle, E.P., 2006. MODTRAN5: 2006 Update. In, Proceedings of SPIE - The International Society for Optical Engineering, pp. 62331F.
Boyd, I.L., Freer-Smith, P.H., Gilligan, C.A, Godfray, H.C.J., 2013. The consequence of tree pests and diseases for ecosystem services. Science 342, 1235773.
Bright, B.C., Hicke, J.A., Hudak, A.T., 2012. Estimating aboveground carbon stocks of a forest affected by mountain pine beetle in Idaho using lidar and multispectral imagery. Remote Sens. Environ. 124, 270–281.
Brodrick, P.G., Asner, G.P., 2017. Remotely sensed predictors of conifer tree mortality during severe drought. Environ. Res. Lett. 12, 115013.
Byer, S., Jin, Y., 2017. Detecting drought-induced tree mortality in Sierra Nevada forests with time series of satellite data. Remote Sens. 9, 929.
California Department of Water Resources (CDWR), 2010. Governor's Drought Declaration. Resources, California Department of Water.
Carneiro, L.R.D.A., Lima, A.P., Machado, R.B., Magnusson, W.E., 2016. Limitations to the use of species-distribution models for environmental-impact assessments in the Amazon. PLoS One 11, 1–17.
Chen, G., Meentemeyer, R.K., 2016. Remote sensing of forest damage by diseases and insects. In: Weng, Q. (Ed.), Remote Sensing for Sustainability. CRC Press, Taylor & Francis Group, Boca Raton, Florida, pp. 145–162.
Chen, G., Hay, G.J., St-Onge, B., 2012. A GEOBIA framework to estimate forest parameters from lidar transects, Quickbird imagery and machine learning: a case study in Quebec. Canada. Int. J. Appl. Earth Obs. Geoinf. 15, 28–37.
Chen, G., Metz, M.R., Rizzo, D.M., Dillon, W.W., Meentemeyer, R.K., 2015a. Object-based assessment of burn severity in diseased forests using high-spatial and high-spectral resolution MASTER airborne imagery. ISPRS J. Photogramm. Remote Sens. 102, 38–47.
Chen, G., Metz, M.R., Rizzo, D.M., Meentemeyer, R.K., 2015b. Mapping burn severity in a disease-impacted forest landscape using Landsat and MASTER imagery. Int. J. Appl. Earth Obs. Geoinf. 40, 91–99.
Chen, G., He, Y., De Santis, A., Li, G., Cobb, R., Meentemeyer, R.K., 2017. Assessing the impact of emerging forest disease on wildfire using Landsat and KOMPSAT-2 data. Remote Sens. Environ. 195, 218–229.
Clark, R. N., Swayze, G. A., Livo, K. E., Kokaly, R. F., King, T. V. V., Dalton, J. B., Vance, J. S., Rockwell, B.W., Hoefen, T. and McDougal, R.R., 2002. Surface reflectance calibration of terrestrial imaging spectroscopy data: a tutorial using AVIRIS. In R. O. Green (Ed.), Proceedings of the 10th JPL Airborne Science Workshop: JPL Publication 02-1. Available online at http://speclab.cr.usgs.gov/PAPERS.calibration.tutorial(last accessed on March 20, 2019).
Coops, N.C., Johnson, M., Wulder, M.A., White, J.C., 2006. Assessment of QuickBird high spatial resolution imagery to detect red attack damage due to mountain pine beetle infestation. Remote Sens. Environ. 103, 67–80.
Cunniffe, N.J., Cobb, R.C., Meentemeyer, R.K., Rizzo, D.M., Gilligan, C.A., 2016. Modeling when, where, and how to manage a forest epidemic, motivated by sudden oak death in California. Proc. Natl. Acad. Sci. 113, 5640–5645.
Davidson, J.M., Wickland, A.C., Patterson, H.A., Falk, K.R., Rizzo, D.M., 2005. Transmission of Phytophthora ramorum in mixed-evergreen forest in California. Phytopathology 95, 587–596.
Davis, F.W., Borchert, M., Meentemeyer, R.K., Flint, A., Rizzo, D.M., 2010. Pre-impact forest composition and ongoing tree mortality associated with sudden oak death in the Big Sur region. California. For. Ecol. Manage. 259, 2342–2354.
Dennison, P.E., Halligan, K.Q., Roberts, D.A., 2004. A comparison of error metrics and constraints for multiple endmember spectral mixture analysis and spectral angle mapper. Remote Sens. Environ. 93, 359–367.
Dubayah, R.C., 1994. Modeling a solar radiation topoclimatology for the Rio Grande River Basin. J. Veg. Sci. 5, 627–640.
Elith, J., Leathwick, J.R., 2009. Species distribution models: ecological explanation and prediction across space and time. Annu. Rev. Ecol. Evol. Syst. 40, 677–697.
Fassnacht, F.E., Latifi, H., Ghosh, A., Joshi, P.K., Koch, B., 2014. Assessing the potential of hyperspectral imagery to map bark beetle-induced tree mortality. Remote Sens. Environ. 140, 533–548.
Fischer, D.T., Still, C.J., Williams, A.P., 2009. Significance of summer fog and overcast for drought stress and ecological functioning of coastal California endemic plant species. J. Biogeogr. 36, 783–799.
Franklin, J., 1995. Predictive vegetation mapping: geographic modelling of biospatial patterns in relation to environmental gradients. Prog. Phys. Geogr. 19, 474–499.
Freeman, E.A., Moisen, G.G., 2008. A comparison of the performance of threshold criteria for binary classification in terms of predicted prevalence and kappa. Ecol. Model. 217, 48–58.
Ghulam, A., Porton, I., Freeman, K., 2014. Detecting subcanopy invasive plant species in tropical rainforest by integrating optical and microwave (InSAR/PolInSAR) remote sensing data, and a decision tree algorithm. ISPRS J. Photogramm. Remote Sens. 88, 174–192.
Hatala, J.A., Crabtree, R.L., Halligan, K.Q., Moorcroft, P.R., 2010. Landscape-scale patterns of forest pest and pathogen damage in the Greater Yellowstone Ecosystem. Remote Sens. Environ. 114, 375–384.
He, K.S., Bradley, B.A., Cord, A.F., Rocchini, D., Tuanmu, M.N., Schmidtlein, S., Turner, W., Wegmann, M., Pettorelli, N., 2015a. Will remote sensing shape the next generation of species distribution models? Remote Sens. Ecol. Conserv. 1, 4–18.
He, T., Liang, S., Wang, D., Shi, Q., Goulden, M.L., 2015b. Estimation of high-resolution land surface net shortwave radiation from AVIRIS data: algorithm development and preliminary results. Remote Sens. Environ. 167, 20–30.
He, Y., Chen, G., De Santis, A., Roberts, D.A., Zhou, Y., Meentemeyer, R.K., 2019. A disturbance weighting analysis model (DWAM) for mapping wildfire burn severity in the presence of forest disease. Remote Sens. Environ. 221, 108–121.
Hultquist, C., Chen, G., Zhao, K., 2014. A comparison of Gaussian process regression, random forests and support vector regression for burn severity assessment in diseased forests. Remote Sens. Lett. 5, 723–732.
Hunter, S., Williams, N., McDougal, R., Scott, P., Garbelotto, M., 2018. Evidence for rapid adaptive evolution of tolerance to chemical treatments in Phytophthora species and its practical implications. PLoS One 13 (12), e0208961.
Ivors, K., Garbelotto, M., Vries, I.D.E., Ruyter-Spira, C., Te Hekkert, B., Rosenzweig, N., Bonants, P., 2006. Microsatellite markers identify three lineages of Phytophthora ramorum in US nurseries, yet single lineages in US forest and European nursery populations. Mol. Ecol. 15, 1493–1505.
Kelly, M., Meentemeyer, R.K., 2002. Landscape dynamics of the spread of sudden oak death. Photogramm. Eng. Remote. Sens. 68, 1001–1009.
Kelly, M., Shaari, D., Guo, Q.H., Liu, D., 2004. A comparison of standard and hybrid classifier methods for mapping hardwood mortality in areas affected by “sudden oak death.” Photogramm. Eng. Remote Sensing 70, 1229–1239.
Kelly, M., Guo, Q., Liu, D., Shaari, D., 2007. Modeling the risk for a new invasive forest disease in the United States: an evaluation of five environmental niche models. Comput. Environ. Urban Syst. 31, 689–710.
Likens, G., Bormann, F., Johnson, N., 1981. Interactions between major biogeochemical cycles in terrestrial ecosystems. In: Likens, G. (Ed.) Some Perspectives of the Major Biogeochemical Cyclespp, pp. 93–112.
Liu, D., Kelly, M., Gong, P., 2006. A spatial-temporal approach to monitoring forest disease spread using multi-temporal high spatial resolution imagery. Remote Sens. Environ. 101, 167–180.
Liu, D., Kelly, M., Gong, P., Guo, Q., 2007. Characterizing spatial-temporal tree mortality patterns associated with a new forest disease. For. Ecol. Manage. 253, 220–231.
McDowell, N., Allen, C.D., Anderson-Teixeira, K., Brando, P., Brienen, R., Chambers, J., Christoffersen, B., Davies, S., Doughty, C., Duque, A., Espirito-Santo, F., 2018. Drivers and mechanisms of tree mortality in moist tropical forests. New Phytol. 219, 851–869.
McGarigal, K., 2014. FRAGSTATS Help. University of Massachusetts, Amherst, MA (209 pp.).
McGarigal, K., Marks, B.J., 1995. FRAGSTATS: Spatial Pattern Analysis Program for Quantifying Landscape Structure. U.S. Department of Agriculture Forest Service. Pacific Northwest Research Station, Portland, OR, p. 122. Report nr Gen. Tech. Re. PNW-GTR-351.
Meddens, A.J.H., Hicke, J.A., Vierling, L.A., 2011. Evaluating the potential of multispectral imagery to map multiple stages of tree mortality. Remote Sens. Environ. 115, 1632–1642.
Meddens, A.J.H., Hicke, J.A., Vierling, L.A., Hudak, A.T., 2013. Evaluating methods to detect bark beetle-caused tree mortality using single-date and multi-date Landsat imagery. Remote Sens. Environ. 132, 49–58.
Meentemeyer, R.K., Anacker, B.L., Mark, W., Rizzo, D.M., 2008a. Early detection of emerging forest disease using dispersal estimation and ecological niche modeling. Ecol. Appl. 18, 377–390.
Meentemeyer, R.K., Rank, N.E., Shoemaker, D.A., Oneal, C.B., Wickland, A.C., Frangioso, K.M., Rizzo, D.M., 2008b. Impact of sudden oak death on tree mortality in the Big Sur ecoregion of California. Biol. Invasions 10, 1243–1255.
Meentemeyer, R.K., Cunniffe, N.J., Cook, A.R., Filipe, J.A.N., Hunter, R.D., Rizzo, D.M., Gilligan, C.A., 2011. Epidemiological modeling of invasion in heterogeneous landscapes: spread of sudden oak death in California (1990–2030). Ecosphere 2, art17.
Meentemeyer, R.K., Dorning, M.A., Vogler, J.B., Schmidt, D., Garbelotto, M., 2015. Citizen science helps predict risk of emerging infectious disease. Front. Ecol. Environ. 13, 189–194.
Moore, I.D., Grayson, R.B., Ladson, A.R., 1991. Digital terrain modeling: a review of hydrological geomorphological and biological applications. Hydrol. Process. 5, 3–30.
NASA, 2018. Landsat Science. https://landsat.gsfc.nasa.gov/landsat-data-continuity-mission/(last accessed on March 20, 2019).
Negrón-Juárez, R.I., Holm, J.A., Marra, D.M., Rifai, S.W., Riley, W.J., Chambers, J.Q., Koven, C.D., Knox, R.G., McGroddy, M.E., Di Vittorio, A.V., Urquiza-Muñoz, J., 2018. Vulnerability of Amazon forests to storm-driven tree mortality. Environ. Res. Lett. 13, 054021.
Pasquarella, V.J., Bradley, B.A., Woodcock, C.E., 2017. Near-real-time monitoring of insect defoliation using Landsat time series. Forests 8, 275.
Paz-Kagan, T., Brodrick, P.G., Vaughn, N.R., Das, A.J., Stephenson, N.L., Nydick, K.R., Asner, G.P., 2017. What mediates tree mortality during drought in the southern Sierra Nevada? Ecol. Appl. 27, 2443–2457.
Potere, D., 2008. Horizontal positional accuracy of Google Earth's high-resolution imagery archive. Sensors 8, 7973–7981.
Potter, C., 2016. Landscape patterns of burn severity in the soberanes fire of 2016. J. Geogr. Nat. Disast. S6, 005. https://doi.org/10.4172/2167–0587.S6-005.
Prospero, S., Hansen, E.M., Grünwald, N.J., Winton, L.M., 2007. Population dynamics of the sudden oak death pathogen Phytophthora ramorum in Oregon from 2001 to 2004. Mol. Ecol. 16, 2958–2973.
R Core Team, 2017. R: A Language and Environment for Statistical Computing. R Foundation for Statistical Computing, Vienna, Austria URL. https://www.r-project.org/, Accessed date: 20 March 2019.
Rizzo, D.M., Garbelotto, M., Davidson, J.M., Slaughter, G.W., Koike, S.T., 2002. Phytophthora ramorum as the cause of extensive mortality of Quercus spp. and

Lithocarpus densiflorus in California. Plant Dis. 86, 205–214.
Rizzo, D.M., Garbelotto, M., Hansen, E.M., 2005. Phytophthora ramorum: integrative research and management of an emerging pathogen in California and Oregon forests. Annu. Rev. Phytopathol. 43, 309–335.
Roberts, D.A., Gardner, M., Church, R., Ustin, S., Scheer, G., Green, R.O., 1998. Mapping chaparral in the Santa Monica Mountains using multiple endmember spectral mixture models. Remote Sens. Environ. 65, 267–279.
Roberts, D.A., Dennison, P.E., Gardner, M.E., Hetzel, Y., Ustin, S.L., Lee, C.T., 2003. Evaluation of the potential of Hyperion for fire danger assessment by comparison to the airborne visible/infrared imaging spectrometer. IEEE Trans. Geosci. Remote Sens. 41, 1297–1310.
Roberts, D.A., Halligan, K., Dennison, P., 2007. VIPER Tools User Manual. V1.5.
Rocchini, D., Andreo, V., Förster, M., Garzon-Lopez, C.X., Gutierrez, A.P., Gillespie, T.W., Hauffe, H.C., He, K.S., Kleinschmit, B., Mairota, P., Marcantonio, M., 2015. Potential of remote sensing to predict species invasions: a modelling perspective. Prog. Phys. Geogr. 39, 283–309.
Roy, D.P., Wulder, M.A., Loveland, T.R., Woodcock, C.E., Allen, R.G., Anderson, M.C., Helder, D., Irons, J.R., Johnson, D.M., Kennedy, R.E., Scambos, T.A., Schaaf, C.B., Schott, J.R., Sheng, Y., Vermote, E.F., Belward, A.S., Bindschadler, R., Cohen, W.B., Gao, F., Hipple, J.D., Hostert, P., Huntington, J., Justice, C.O., Kilic, A., Kovalskyy, V., Lee, Z.P., Lymburner, L., Masek, J.G., McCorkel, J., Shuai, Y., Trezza, R., Vogelmann, J., Wynne, R.H., Zhu, Z., 2014. Landsat-8: science and product vision for terrestrial global change research. Remote Sens. Environ. 145, 154–172.
Rullan-Silva, C.D., Olthoff, A.E., de la Mata, J.A.D., Pajares-Alonso, J.A., 2013. Remote monitoring of forest insect defoliation-a review. Forest Syst. 22, 377–391.
Saatchi, S., Buermann, W., ter Steege, H., Mori, S., Smith, T.B., 2008. Modeling distribution of Amazonian tree species and diversity using remote sensing measurements. Remote Sens. Environ. 112, 2000–2017.
Sansford, C.E., Inman, A.J., Baker, R., Brasier, C., Frankel, S., de Gruyter, J., Husson, C., Kehlenbeck, H., Kessel, G., Moralejo, E., Steeghs, M., Webber, J., Werres, S., 2008. Report on the risk of entry, establishment, spread and socio-economic loss and environmental impact and the appropriate level of management for Phytophthora ramorum for the EU. In: Deliverable Report 28. RAPRA, EU Sixth Framework Project.
Shirk, A.J., Lopez-Sanchez, C.A., Toney, C., Cushman, S.A., Wehenkel, C.A., Leal-Sáenz, A., Waring, K.M., 2018. Southwestern white pine (*Pinus strobiformis*) species distribution models project a large range shift and contraction due to regional climatic changes. For. Ecol. Manage. 411, 176–186.
Skowronek, S., Ewald, M., Isermann, M., Van De Kerchove, R., Lenoir, J., Aerts, R., Warrie, J., Hattab, T., Honnay, O., Schmidtlein, S., Rocchini, D., 2017. Mapping an invasive bryophyte species using hyperspectral remote sensing data. Biol. Invasions 19, 239–254.
Sturrock, R.N., Frankel, S.J., Brown, A.V., Hennon, P.E., Kliejunas, J.T., Lewis, K.J., Worrall, J.J., Woods, A.J., 2011. Climate change and forest diseases. Plant Pathol. 60, 133–149.
Thornton, M.M., Thornton, P.E., Wei, Y., Mayer, B.W., Cook, R.B., Vose, R.S., 2018. Daymet: Monthly Climate Summaries on a 1-km Grid for North America, Version 3. ORNL DAAC, Oak Ridge, Tennessee, USA.
Turner, M.G., Gardner, R.H., O'Neill, R.V., 2001. Landscape Ecology in Theory and Practice: Pattern and Process. Springer.
U.S. Geological Survey, 2017. California Drought. U.S. Geological Survey, California Water Science Center.
U.S. Geological Survey, 2018a. Landsat 4–7 Surface Reflectrance (LEDAPS) Product.
U.S. Geological Survey, 2018b. Landsat 8 Surface Reflectrance Code (LaSRC) Product.
USDA, 2012. National Agriculture Imagery Program (NAIP) Orthoimagery. Available online: https://www.fsa.usda.gov/Internet/FSA_File/naip_2012_infosheet.pdf(last accessed on March 20, 2019).
Václavík, T., Meentemeyer, R.K., 2009. Invasive species distribution modeling (iSDM): are absence data and dispersal constraints needed to predict actual distributions? Ecol. Modell. 220, 3248–3258.
Vaughn, N.R., Asner, G.P., Brodrick, P.G., Martin, R.E., Heckler, J.W., Knapp, D.E., Hughes, R.F., 2018. An approach for high-resolution mapping of Hawaiian metrosideros forest mortality using laser-guided imaging spectroscopy. Remote Sens. 10, 502.
Wingfield, M.J., Brockerhoff, E.G., Wingfield, B.D., Slippers, B., 2015. Planted forest health: the need for a global strategy. Science 349, 832–836.